We are IntechOpen, the world's leading publisher of Open Access books Built by scientists, for scientists

6,900
Open access books available

185,000
International authors and editors

200M
Downloads

Our authors are among the

154
Countries delivered to

TOP 1%
most cited scientists

12.2%
Contributors from top 500 universities



WEB OF SCIENCE™

Selection of our books indexed in the Book Citation Index in Web of Science™ Core Collection (BKCI)

Interested in publishing with us?
Contact book.department@intechopen.com

Numbers displayed above are based on latest data collected.
For more information visit www.intechopen.com



1

Numerical Simulation of the Bump-on-Tail Instability

Magdi Shoucri
Institut de recherche Hydro-Québec (IREQ), Varennes, Québec J3X1S1, Canada

1. Introduction

Wave-particle interaction is among the most important and extensively studied problems in plasma physics. Langmuir waves and their Landau damping or growth are fundamental examples of wave-particle interaction. The bump-on-tail instability is an example of wave growth and is one of the most fundamental and basic instabilities in plasma physics. When the bump in the tail of the distribution function presents a positive slope, a wave perturbation whose phase velocity lies along the positive slope of the distribution function becomes unstable. The bump-on-tail instability has been generally studied analytically and numerically under various approximations, either assuming a cold beam, or the presence of a single wave, or assuming conditions where the beam density is weak so that the unstable wave representing the collective oscillations of the bulk particles exhibits a small growth and can be considered as essentially of slowly varying amplitude in an envelope approximation (see for instance Umeda *et al*., 2003, Doveil *et al*. 2001, and references therein). Some early numerical simulations have studied the growth, saturation and stabilization mechanism for the beam-plasma instability (Dawson and Shanny, 1968, Denavit and Kruer, 1971, Joyce *et al*., 1971, Nührenberg, 1971). Using Eulerian codes for the solution of the Vlasov-Poisson system (Cheng and Knorr, 1976, Gagné and Shoucri, 1977), it has been possible to present a better picture of the nonlinear evolution of the bump-on-tail instability (Shoucri, 1979), where it has been shown that for a single wave perturbation the initial bump in the tail of the distribution is distorted during the instability, and evolves to an asymptotic state having another bump in the tail of the spatially averaged distribution function, with a minimum of zero slope at the phase velocity of the initially unstable wave (in this way the large amplitude wave can oscillate at constant amplitude without growth or damping). The phase-space in this case shows in the asymptotic state a Bernstein-Greene-Kruskal (BGK) vortex structure traveling at the phase-velocity of the wave (Bernstein *et al*., 1957, Bertrand *et al*., 1988, Buchanan and Dorning, 1995). These results are also confirmed in several simulations (see for instance Nakamura and Yabe, 1999, Crouseilles *et al*., 2009). Since the early work of Berk and Roberts, 1967, the existence of steady-state phase-space holes in plasmas has been discussed in several publications. A discussion on the formation and dynamics of coherent structures involving phase-space holes in plasmas has been presented for instance in the recent works of Schamel, 2000, Eliasson and Shukla, 2006.
There are of course situations where a single wave theory and a weak beam density do not apply. In the present Chapter, we present a study for the long-time evolution of the Vlasov-

Poisson system for the problem of the bump-on-tail instability, for the case when the beam density is about 10% of the total density, which provides a more vigorous beam-plasma interaction and important wave-particle and trapped particles effects. In this case the instability and trapping oscillations have important feedback effects on the oscillation of the bulk. Since the bump in the tail is usually located in the low density region of the distribution function, the Eulerian codes, because of their low noise level, allow an accurate study of the evolution of the bump, and on the transient dynamics for the formation and representation of the traveling BGK structures (for details on the numerical codes see the recent articles in Pohn *et al*., 2005, Shoucri, 2008, 2009). A warm beam is considered, and the system length L is greater than the wavelength of the unstable mode λ. In this case growing sidebands develop with energy flowing to the longest wavelengths (inverse cascade). This inverse cascade is characteristic of 2D systems (Knorr, 1977). Oscillations at frequencies below the plasma frequency are associated with the longest wavelengths, and result in phase velocities above the initial beam velocity, trapping and accelerating particles to higher velocities. The electric energy of the system is reaching in the asymptotic state a steady state with constant amplitude modulated by the persistent oscillation of the trapped particles, and of particles which are trapped, untrapped and retrapped. A similar problem has been recently studied in Shoucri, 2010. In the present chapter, we shall consider a larger simulation box, capable of resolving a broader spectrum. Two cases will be studied. A case where a single unstable mode is initially excited, and a case where two unstable modes are initially excited. Differences in the results between these two cases will be pointed out.

The transient dynamics of the Vlasov-Poisson system is sensitive to grid size effects (see, for instance, Shoucri, 2010, and references therein). Numerical grid size effects and small time-steps can have important consequences on the number and distribution of the trapped particles, on kinetic microscopic processes such as the chaotic trajectories which appear in the resonance region at the separatrix of the vortex structures where particles can make periodic transitions from trapped to untrapped motion. Usually during the evolution of the system, once the microstructure in the phase-space is reaching the mesh size, it is smoothed away by numerical diffusion, and is therefore lost. Larger scales appear to be unaffected by the small scale diffusivity and appear to be treated with good accuracy. This however has consequences on smoothing out information on trapped particles, and modifying some of the oscillations associated with these trapped particles, and with particles at the separatrix region of the vortex structures which evolve periodically between trapping and untrapping states. These trapped particles play an important role in the macroscopic nonlinear oscillation and modulation of the asymptotic state, and require a fine resolution phase-space grid and a very low noise code to be studied as accurately as possible (Califano and Lantano, 1999, Califano *et al*., 2000, Doveil *et al*., 2001, Valentini *et al*., 2005, Shoucri, 2010).

The transient dynamics of the Vlasov-Poisson system is also sensitive to the initial perturbation of the system. Two cases will be considered in this chapter in the context of the bump-on-tail instability. A case where a single unstable mode is initially excited, and a case where two unstable modes are initially excited. In the first case, the system reaches in a first stage a BGK traveling wave, which in this case with $L > \lambda$ is only an intermediate state. Growing sidebands develop which disrupt the BGK structure and the system evolves in the end to a phase-space hole which translates as a cavity-like structure in the density plot. In the case where two initially unstable modes are excited, the electric energy decays rapidly after the initial growth and the vortices formed initially are unstable, and the phase-space evolves rapidly to a structure with a hole. In both cases energy is transferred by inverse

cascade to the longest wavelengths available in the system. A more important heating of the tail is observed in this second case.

2. The relevant equations

The relevant equations are the 1D Vlasov equation for the electron and ion distribution functions $f_e(x,\upsilon_e,t)$ and $f_i(x,\upsilon_i,t)$, coupled to the Poisson equation. These equations are written in our normalized units:

$$\frac{\partial f_{e,i}}{\partial t}+\frac{\partial f_{e,i}}{\partial x}\mp\frac{1}{m_{e,i}}E_x\frac{\partial f_{e,i}}{\partial \upsilon_{e,i}}=0 \tag{1}$$

$$\frac{\partial^2\varphi}{\partial x^2}=-(n_i(x)-n_e(x))\;;\; n_{e,i}(x)=\int_{-\infty}^{+\infty} f_{e,i}(x,\upsilon_{e,i})d\upsilon_{e,i} \tag{2}$$

$$E_x=-\frac{\partial\varphi}{\partial x} \tag{3}$$

Time t is normalized to the inverse electron plasma frequency ω_{pe}^{-1}, velocity is normalized to the electron thermal velocity $\upsilon_{the}=\sqrt{T_e/m_e}$ and length is normalized to the Debye length $\lambda_{D_e}=\upsilon_{the}/\omega_{pe}$. In our normalized units, $m_e=1$ and $m_i=M_i/M_e$. Periodic boundary conditions are used. These equations are discretized on a grid in phase-space and are solved with an Eulerian code, by applying a method of fractional step which has been previously presented in the literature (Cheng and Knorr, 1976, Gagné and Shoucri, 1977, Shoucri, 2008, 2009). The distribution function for a homogeneous electron beam-plasma system, with an electron beam drifting with a velocity υ_d relative to a stationary homogeneous plasma is given by:

$$f_e(\upsilon_e)=\frac{n_p}{\sqrt{2\pi}}e^{-\frac{1}{2}\upsilon_e^2}+\frac{n_b}{\sqrt{2\pi}\upsilon_{thb}}e^{-\frac{1}{2}\frac{(\upsilon_e-\upsilon_d)^2}{\upsilon_{thb}^2}} \tag{4}$$

The electron beam thermal spread is $\upsilon_{thb}=0.5$ and the beam velocity is $\upsilon_d=4.5$. The ion distribution function in our normalized units is given by:

$$f_i(\upsilon_i)=\frac{n_i}{\sqrt{2\pi}\upsilon_{thi}}e^{-\frac{1}{2}\upsilon_i^2/\upsilon_{thi}^2} \tag{5}$$

We take for the electron plasma density $n_p=0.9$ and for the electron beam density $n_b=0.1$ for a total density of 1. This high beam density will cause a strong beam-plasma instability to develop. We take $n_i=1.$, $T_e/T_i=1$, $m_e/m_i=1./1836$. In our normalized units $\upsilon_{thi}=\sqrt{T_i m_e/T_e m_i}$. We use a time-step $\Delta t=0.002$. The length of the system in the present simulations is $L=80\text{x}2\pi/3=167.552$.

3. Excitation of the mode n=8 with k=0.3

We perturb the system initially with a perturbation such that:

$$f_e(x,\upsilon_e) = f(\upsilon_e)(1+\varepsilon\cos(kx)) \tag{6}$$

with $\varepsilon = 0.04$ and with $k = n\frac{2\pi}{L}$, and $f_e(\upsilon_e)$ is given in Eq.(4). We consider the case where $k = 0.3$, and the approximate initial frequency response of the system will be $\omega^2 \approx 1 + 3k^2$, or $\omega \approx 1.127$ (nonlinear solutions can give slightly different results) , with a phase velocity of the wave $\omega / k \approx 3.756$. This phase velocity corresponds to a velocity where the initial distribution function in Eq.(4) has a positive slope. Hence the density perturbation in Eq.(6) will lead to an instability. The mode $k = 0.3$ corresponds to the mode with n=8, in which case unstable sidebands can grow (the length of the system is bigger with respect to the wavelength of the excited oscillation). We use a space-velocity grid of 1024x2400 for the electrons, with extrema in the electron velocity equal to ± 8. The recurrence time in this case is $\tau = \frac{2\pi}{k\Delta\upsilon} \approx 3140$. We use a space-velocity grid of 1024x800 for the ions.

Unstable sidebands are growing from round-off errors. Fig.(1) presents the time evolution of the electric energy, showing growth, saturation and trapped particle oscillations until around a time t=700. Figs.(2a,b) show the contour plot and a three-dimensional view at t=680 of the distribution function showing the formation of a stable structure of eight vortices, corresponding to the initially unstable n=8 mode. The frequency spectrum of the mode n=8 at this stage of the evolution of the system shows a dominant frequency at $\omega = 1.0258$ (see Fig.(19b)), corresponding to a phase velocity $\upsilon \approx 3.42$. This corresponds to the velocity at which the center of the BGK structure of in Fig.(2a) is traveling. The spatially averaged distribution function $F_e(\upsilon_e)$ in Fig.(3) is calculated from:

$$F_e(\upsilon_e) = \frac{1}{L}\int_0^L f(x,\upsilon_e)dx \tag{7}$$

The spatially averaged distribution function at this stage of the evolution has evolved from the initial bump-on-tail configuration (full curve in Fig.(3)), to a shape having another bump-on-tail configuration, with a minimum at $\upsilon \approx 3.42$, which corresponds to the phase velocity of the dominant n=8 mode at this stage. So the n=8 mode is reaching at this early stage a constant amplitude modulated by the oscillation of the trapped particles (see Fig.(19a)), with its phase velocity at the local minimum of the spatially averaged distribution function. During this phase of the evolution the spectrum of the n=8 mode in Fig.(19b) shows also the presence of a frequency at $\omega = 1.3134$, which corresponds to a phase velocity $\omega / k = 4.378$, at the local maximum appearing around $\upsilon \approx 4.4$ in the spatially averaged distribution function in Fig.(3). Above $\upsilon \approx 4.4$, the spatially averaged distribution function in Fig.(3) shows a small oscillation with a local minimum due to the trapped population which is apparent above the vortices in Fig.(2a). Fig.(4a) and Fig.(4b) show respectively the electric field and the electron density profiles at t=680.

Then for $t > 700$ there is a rapid decrease in the electric energy down to a constant value, (see Fig.(1)). This is caused by the growing sidebands who have reached a level where they

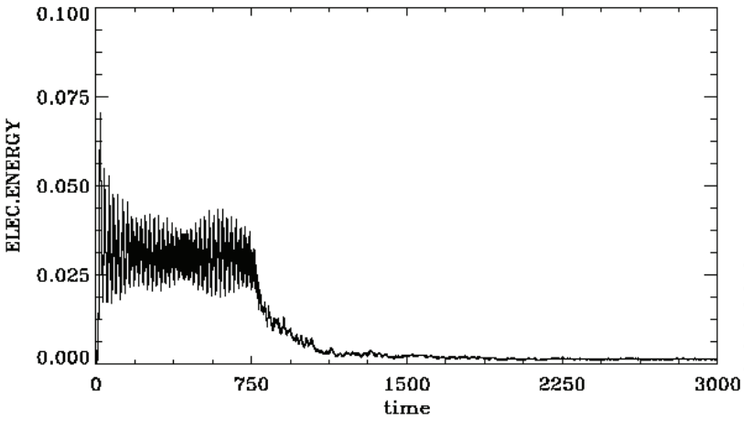
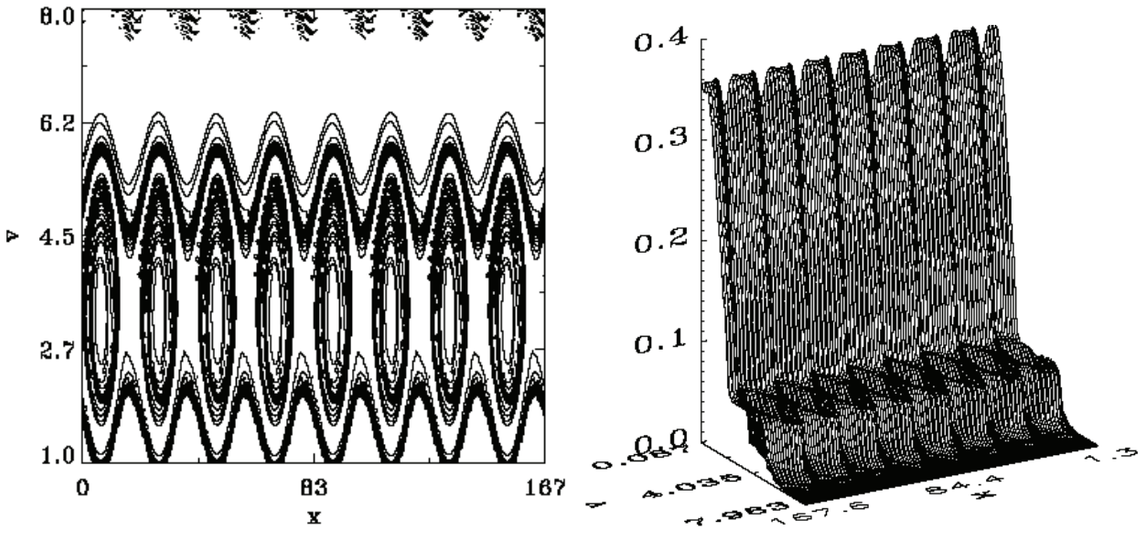


Fig. 1. Time evolution of the electric field energy



(a) (b)

Fig. 2. (a) Contour plot of the distribution function, *t*=680, (b) Three-dimensional view of the distribution function, *t*=680

interact with the eight vortices BGK structure formed. There is a rapid fusion of the vortices into a single vortex, with energy cascading to the longest wavelengths associated with the system, a process characteristic of 2D systems (Knorr,1977). There is a heating of the distribution function, with an elongation of the tail of the distribution. Figs.(5-7) show the sequence of events in the evolution of the phase-space from the eight vortices BGK structure of Fig.(2a) to a single hole structure in Fig.(7o). Fig.(5a) shows at *t*=760 the disruption of the symmetry of the eight vortices structure. Some details are interesting. We note in Fig.(5a) two small vortices, centered around $x \approx 30$ and $x \approx 155$, extending an arm embracing the vortex on their right. We magnify in Fig.(5b) the small vortex centered around $x \approx 30$. Fig.(6a) shows the phase- space at *t*=780. Between Fig.(5a) and Fig.(6a), there is a time delay of 20, in which the structure moves a distance of about $3.42 \text{x} 20 \approx 68$. The small vortex centered at $x \approx 30$ in Figs.(5a,b) has now moved to the position $x \approx 98$ in Fig.(6a).

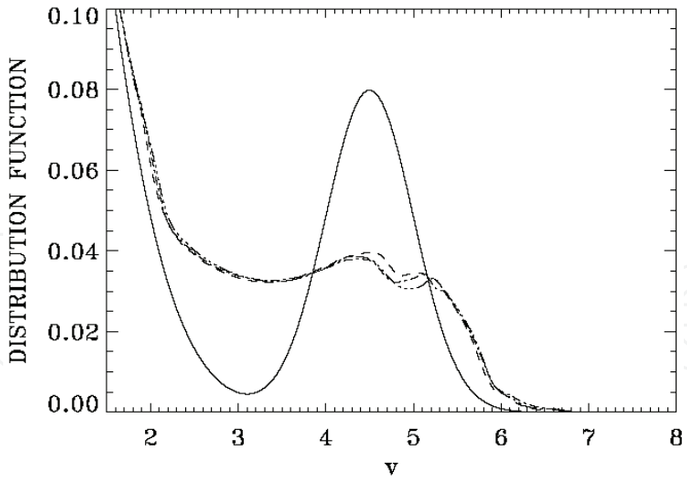
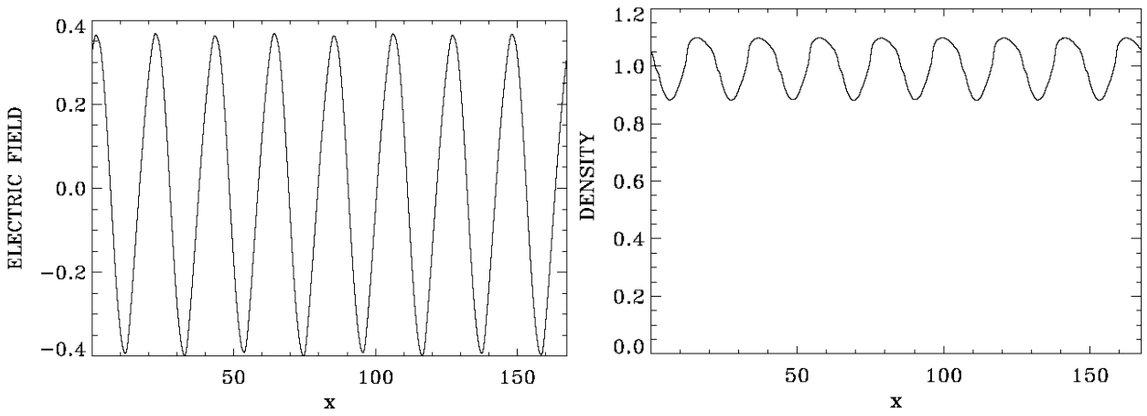


Fig. 3. Spatially averaged distribution function at t=0 (full curve), t=660 (dashed curve), t=680 (dashed-dotted curve), t=700 (dashed-three-dotted curve)



(a) (b)

Fig. 4. (a) Electric field profile at t=680, (b) Electron density profile at t=680

We show in more details in Fig.(6b) these vortices structure which now extend their arms to embrace the neighbouring vortices, both to the right and to the left.

We present in Fig.(7a-o) the sequence of evolution of the phase-space, leading to the formation of a single hole structure in Fig.(7o). Note in Fig.(7g) how the tail of the distribution function has shifted to higher velocities. The sequences in Fig.(7h-o) showing the fusion of the final two vortices is interesting. Fig.(7i) shows that one of the two holes is taking a satellite position with respect to the other one, and then is elongated to form an arm around the central vortex. It appears that the satellite vortex is following a spiral structure around the central vortex, possibly following the separatrix. Fig.(8) shows a 3D view of the distribution function at t=2980, corresponding to the results in Fig.(7o). The center of the hole in the phase-space is traveling at a velocity around ≈ 4.8, which is the phase velocity of the dominant modes in Figs.(12-22), as it will be discussed later on. Note the difference in the structure of the electron distribution function between Fig.(8) and Fig.(2b). In Fig.(8), there is a cavity like structure which extends deep in the bulk and which propagates as a solitary like structure in the phase-space at the phase velocity of the hole.

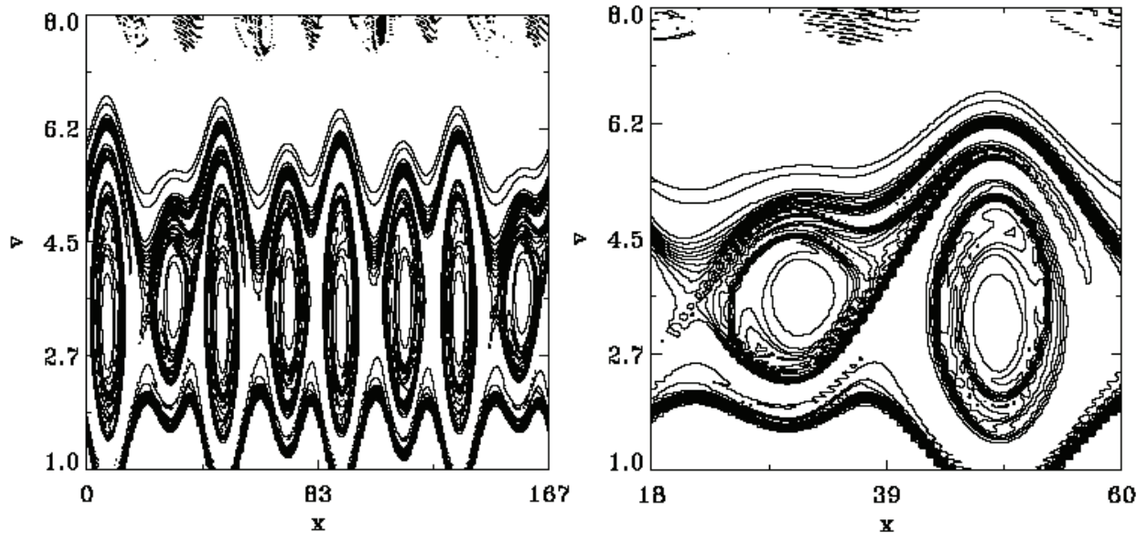


Fig. 5. (a) Contour plot of the distribution function, t=760, (b) same as Fig.5a, figure centered at x=39

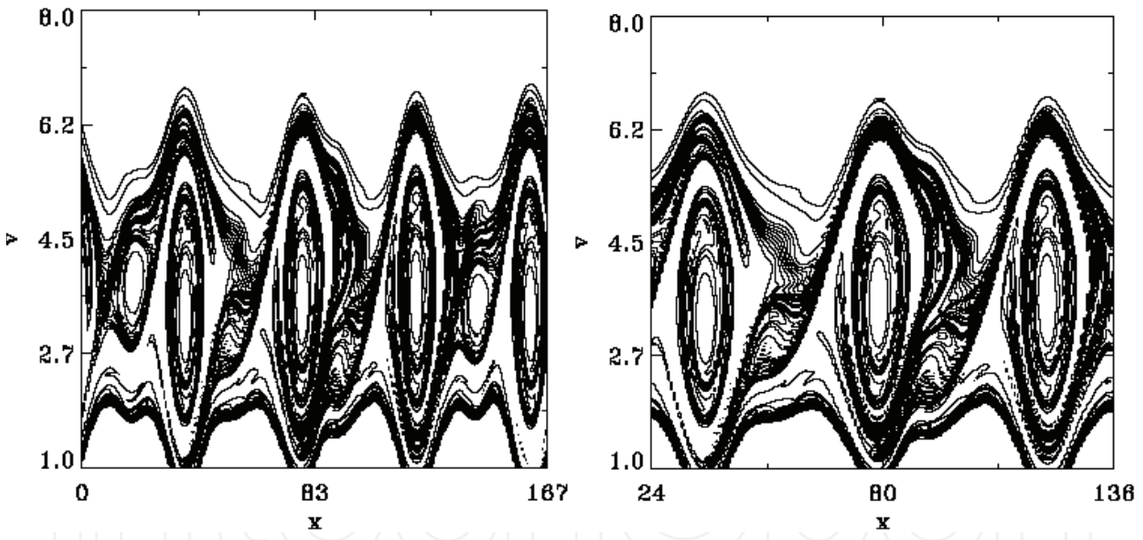


Fig. 6. (a) Contour plot of the distribution function, t=780, (b) same as Fig.6a, centered at x=80

Figs.(9) shows the spatially averaged distribution function for electrons at $t = 2980$, calculated using Eq.(7). Fig.(10) shows the equivalent plot of the ions calculated from an equation equivalent to Eq.(7). Fig.(9) seems to indicate the formation of a plateau. The ion distribution function in Fig.(10) is essentially the same as the initial one at $t = 0$. In Fig.(11a) we plot on a logarithmic scale what appears to be the region of a plateau in Fig.(9). We see in Fig.(11a) the distribution function is decaying slowly, showing an inflexion point around $\upsilon \approx 3.7$, and another one around $\upsilon \approx 4.8$. Fig.(11b) shows on a logarithmic scale a plot of the

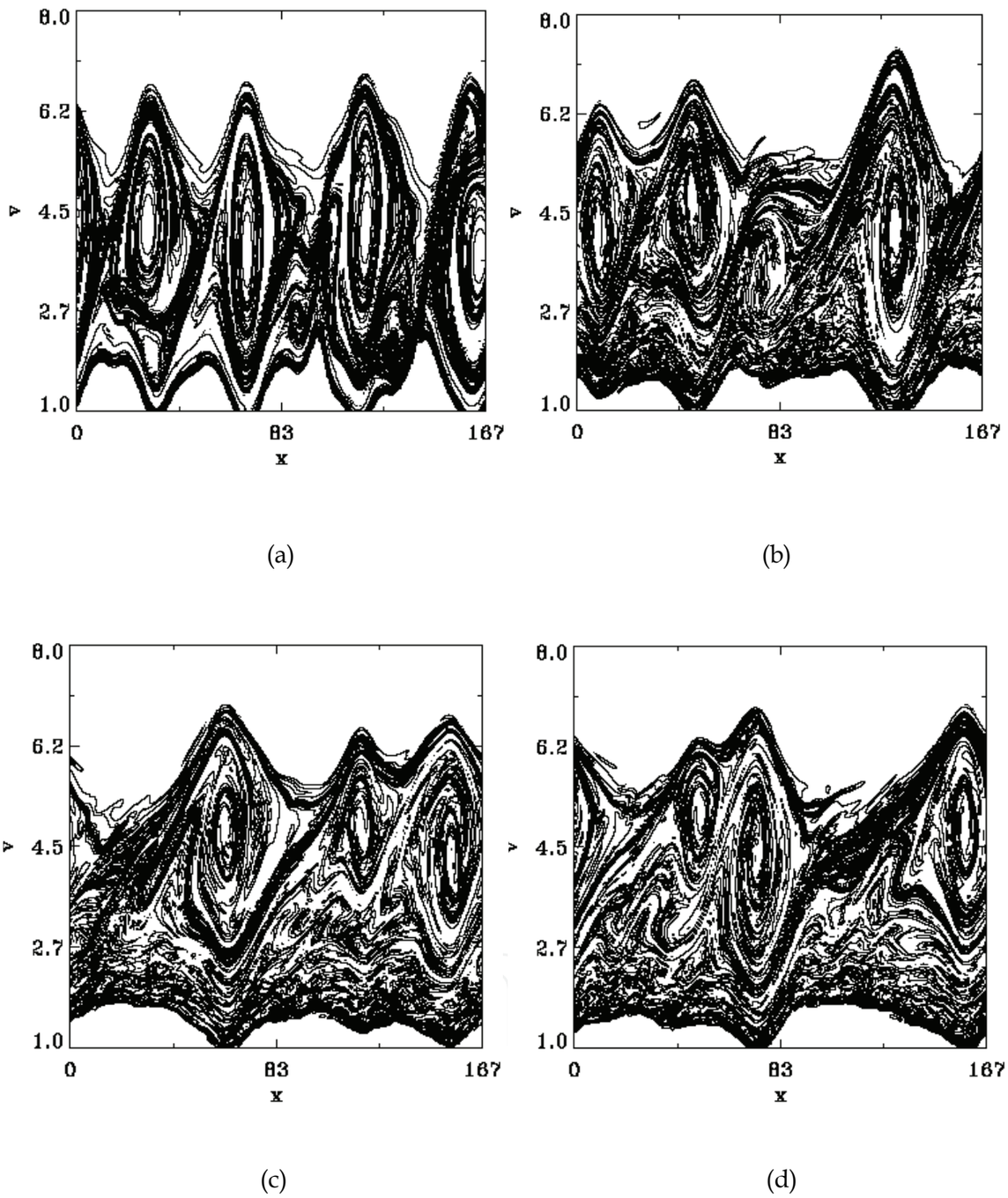
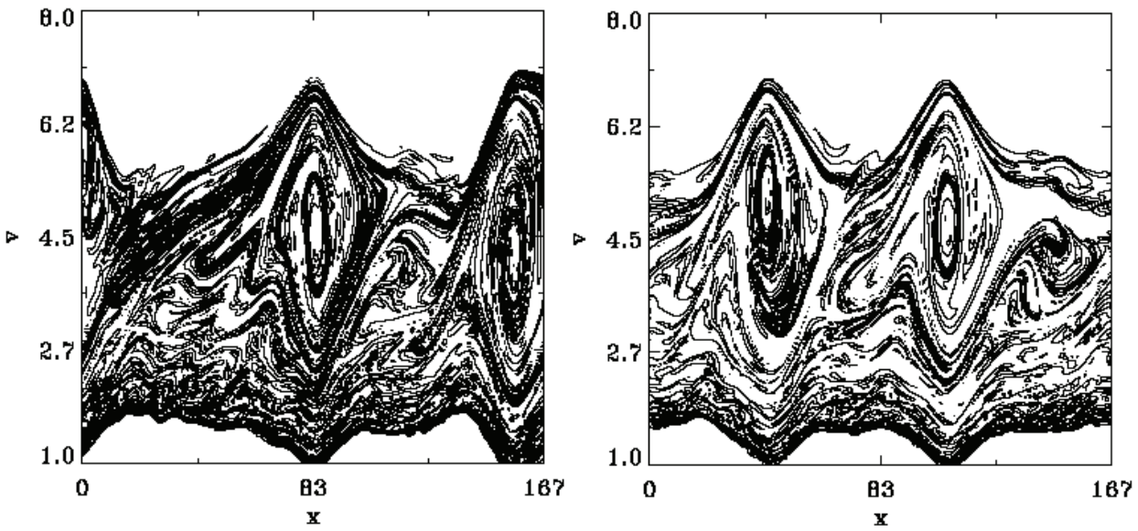
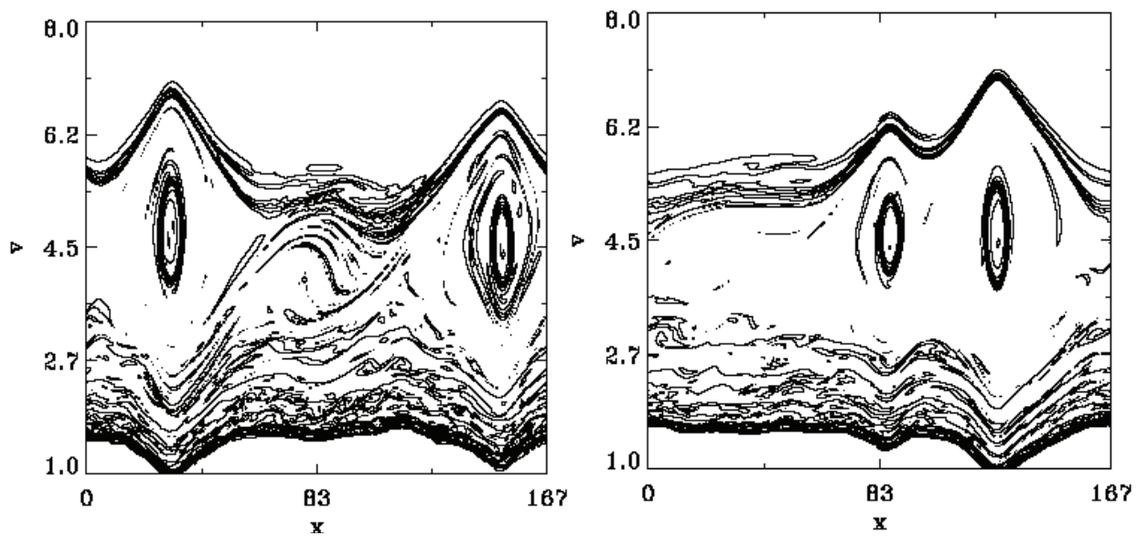


Fig. 7. (a) Contour plot of the distribution function, t=800,
(b) Contour plot of the distribution function, t=1040,
(c) Contour plot of the distribution function, t=1100,
(d) Contour plot of the distribution function, t=1120.

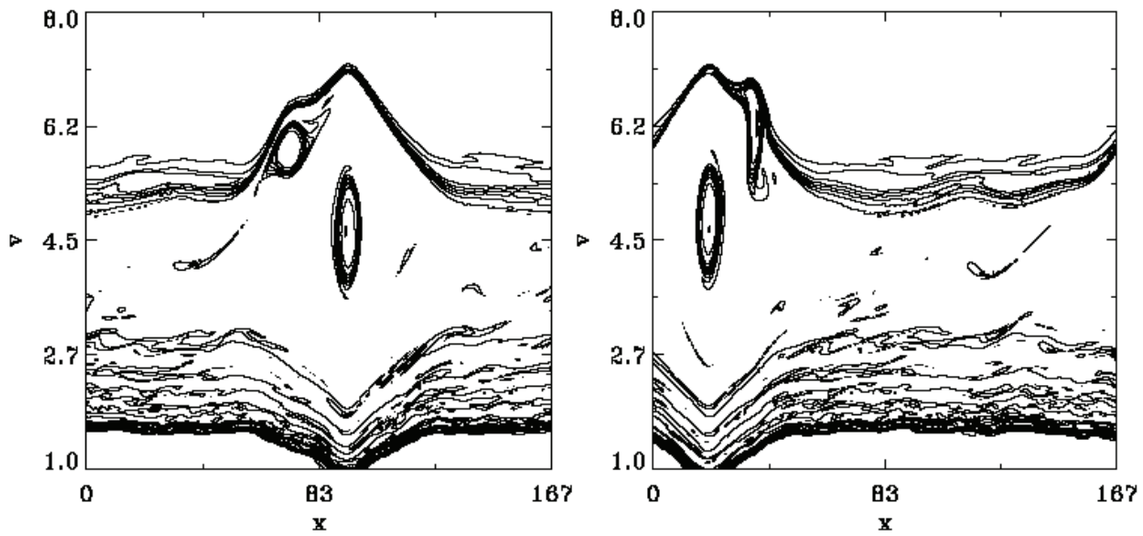


(e) (f)

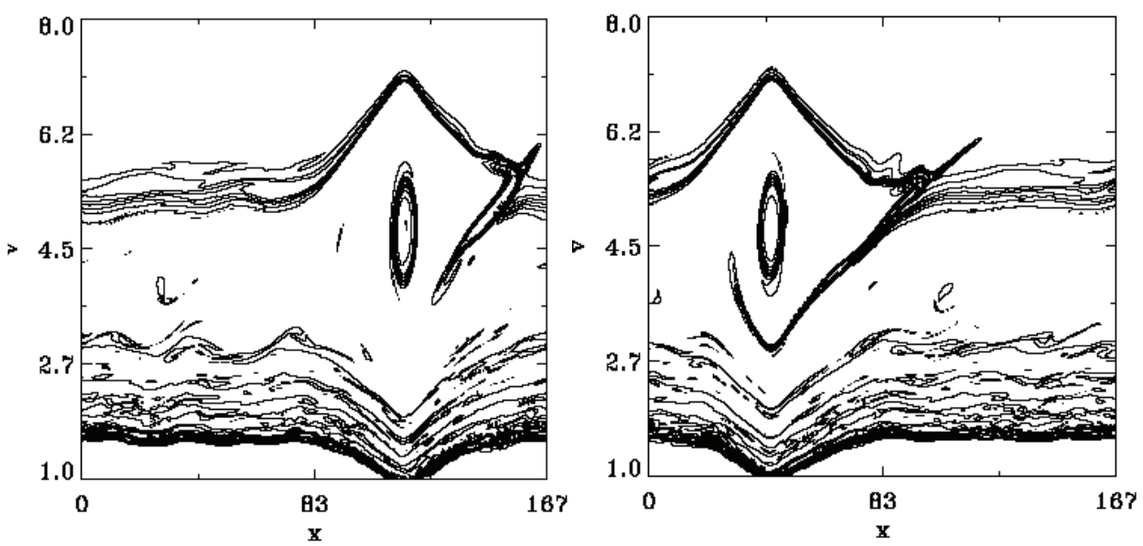


(g) (h)

Fig. 7. (e) Contour plot of the distribution function, t=1140,
(f) Contour plot of the distribution function, t=1400,
(g) Contour plot of the distribution function, t=1600,
(h) Contour plot of the distribution function, t=1800.

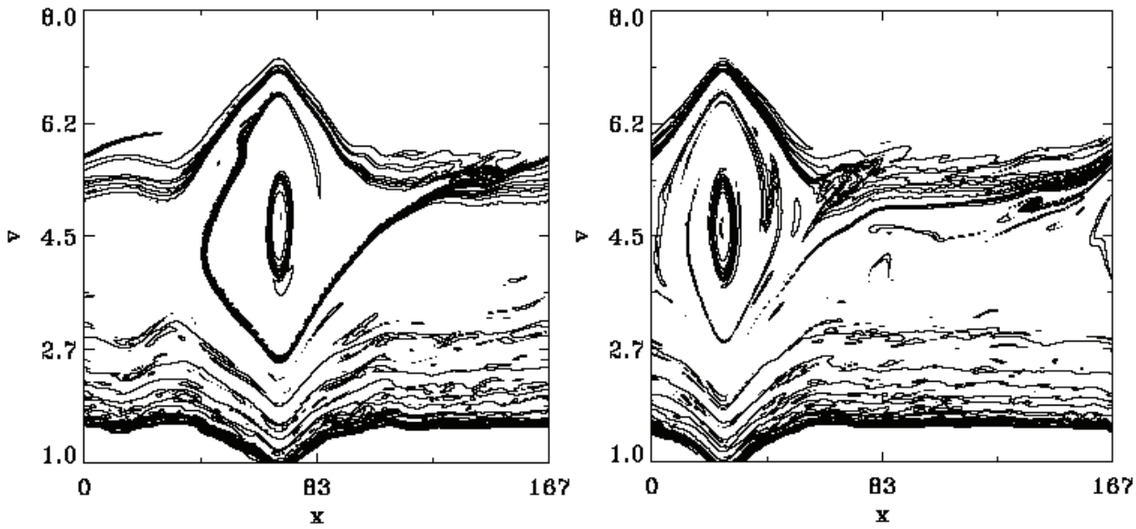


(i) (j)

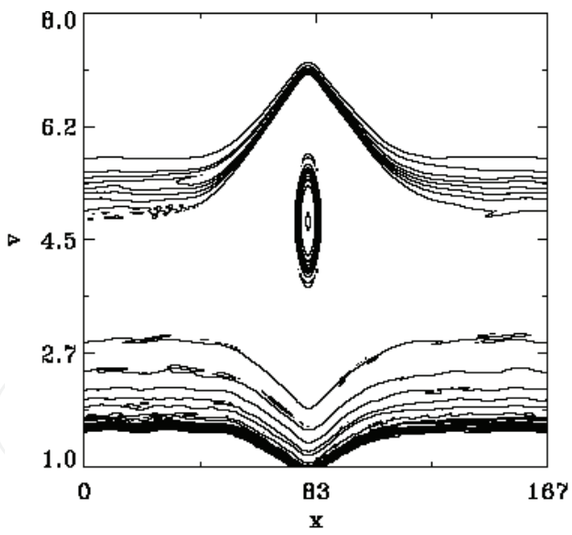


(k) (l)

Fig. 7. (i) Contour plot of the distribution function, t=1900,
(j) Contour plot of the distribution function, t=1920,
(k) Contour plot of the distribution function, t=1940,
(l) Contour plot of the distribution function, t=1960.



(m) (n)



(o)

Fig. 7. (m) Contour plot of the distribution function, t=2000,
(n) Contour plot of the distribution function, t=2200,
(o) Contour plot of the distribution function, t=2980.

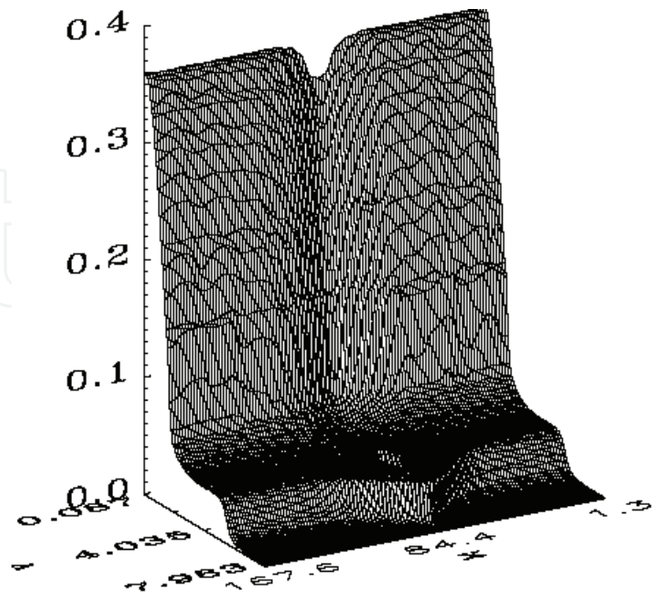


Fig. 8. Three-dimensional view of the results in Fig.7o.

distribution function in the region of the bulk, showing a small knee around $\upsilon \approx 1.1$ and around $\upsilon \approx 1.3$. This corresponds to longitudinal modulations we see in Fig.(8). Fig.(11c) shows, on a linear scale, the top of the electron distribution function, which shows a small cavity around $\upsilon \approx -0.05$. The acoustic speed in our normalized units is $\sqrt{T_e / M_i} / \sqrt{T_e / M_e} = \sqrt{M_e / M_i} \approx 0.023$. In the phase-space plot in Fig.(11d) the structure around $\upsilon \approx -0.05$ shows six vortices, corresponding to a mode with $k = 0.225$.

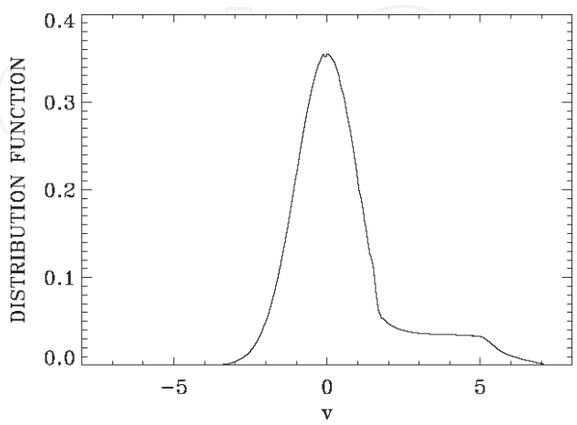


Fig. 9. Electron distribution function at $t = 2980$.

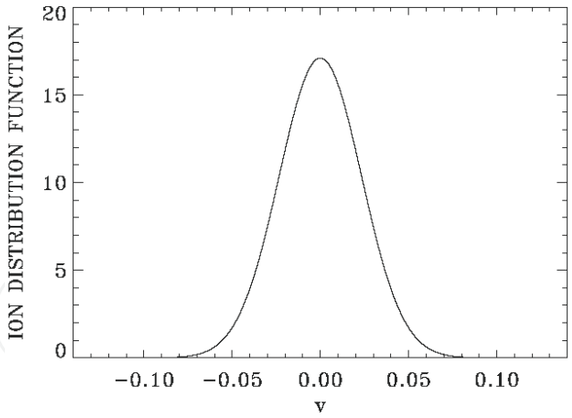


Fig. 10. Ion distribution function at $t = 2980$

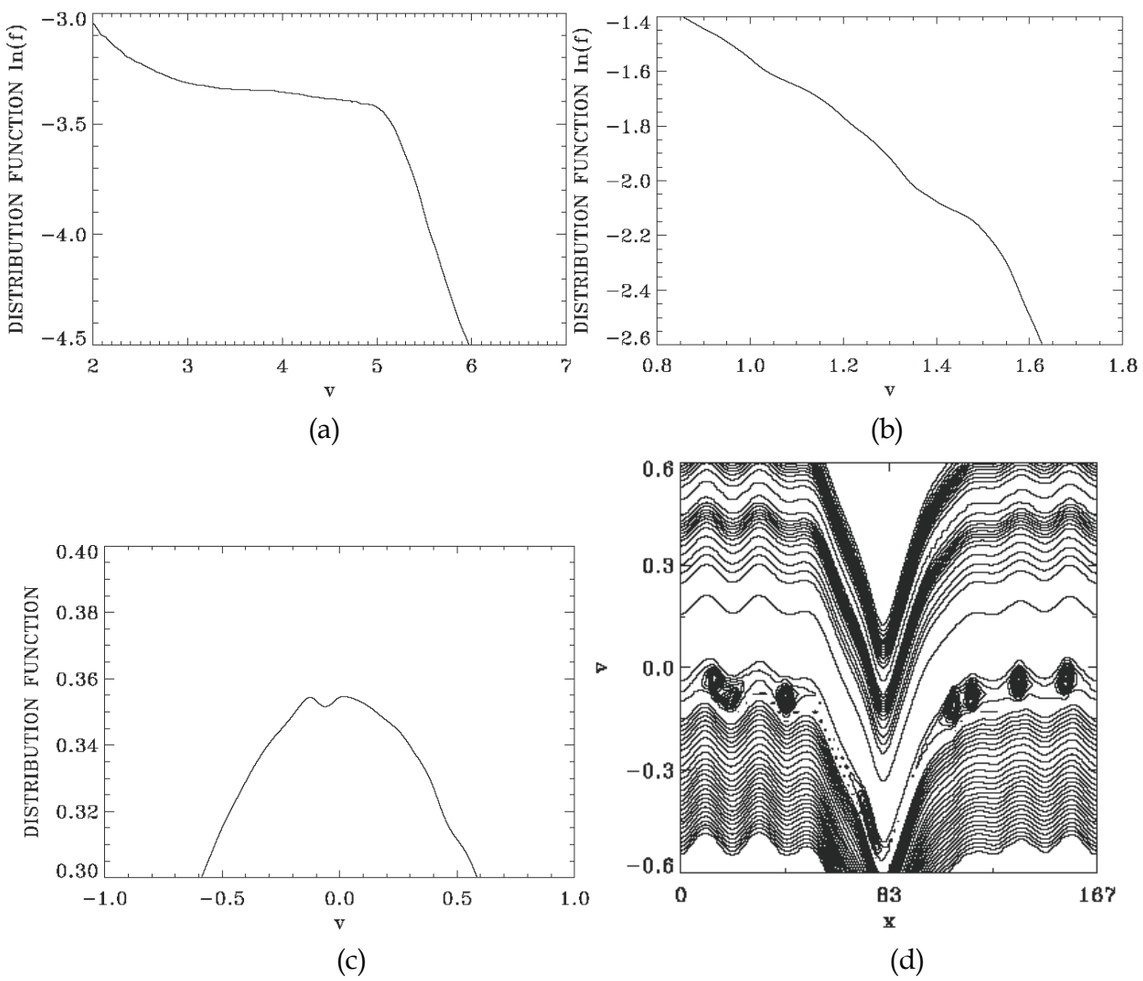
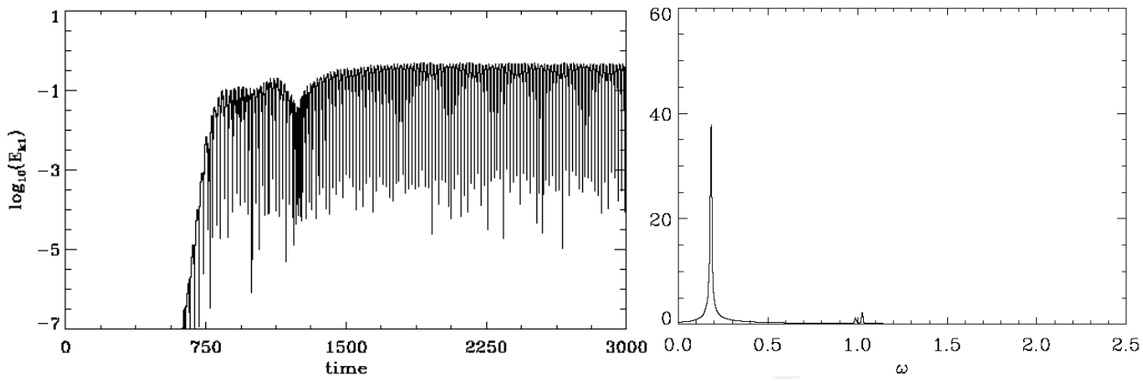


Fig. 11. (a) Same as Fig.(9) (concentrates on the tail)
(b) Same as Fig.(9) (concentrates on the bulk)
(c) Same as Fig.(9) (concentrates on the top)
(d) Contour plot for the distribution in Fig.(11c)

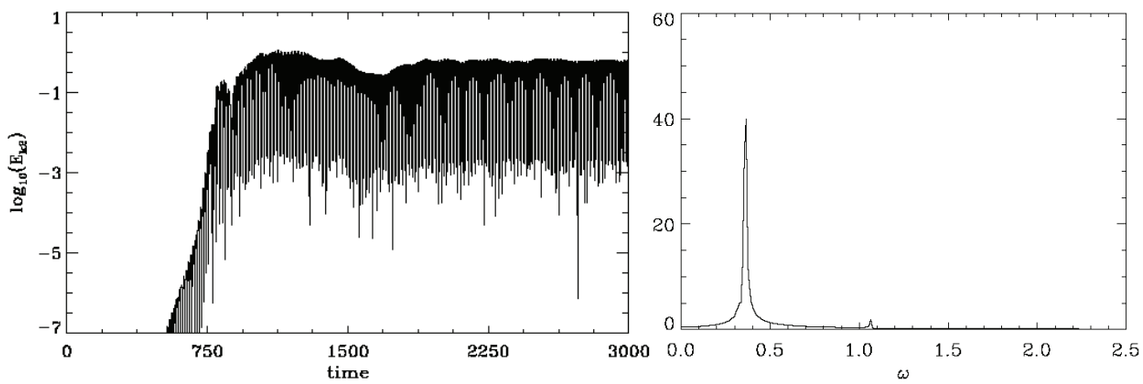
Figs.(12a-19a,20-22) show the time evolution of the different Fourier modes $k = n2\pi / L$ with n =1,2,3,4,5,6,7,8,9,12,16. Fig.(19) shows the initially unstable mode with $k = 0.3$, $n = 8$, growing then saturating (which corresponds to the eight vortices we see in Fig.(2)), and showing trapped particles oscillation. The merging of the vortices in the presence of growing sidebands for $t > 700$ is accompanied by an inverse cascade with a transfer of energy to longest wavelengths. We see the amplitude of the Fourier mode $k = 0.3$, $n = 8$ decreasing sharply for $t > 700$. Also the phase velocity of the center of the final hole in Fig.(7o) for instance has moved higher and is about 4.8, due to the acceleration of the particles during the merging of the vortices. The frequencies of these longest wavelengths are below the plasma frequency. We calculate the frequencies of the different modes by their Fourier transform in the steady state at the end of the evolution, from $t_1 = 2344$ to $t_2 = 3000$. The frequency spectrum of the mode $k = 0.0375$, $n = 1$ given in Fig.(12a) is shown in Fig.(12b), with a peak at $\omega = 0.182$, which corresponds to a phase velocity $\omega / k = 4.853$ around the center of the vortex in Fig.(7o). We have also in Fig.(12b) two very small peaks at $\omega = 0.9875$ and $\omega = 1.0258$, which are modulating the amplitude of the mode. The frequency spectrum of the mode $k = 0.075$, $n = 2$ in Fig.(13a) is given in Fig.(13b), which shows a peak at $\omega = 0.3643$, corresponding to a phase velocity $\omega / k = 4.857$. Another small peak is appearing at $\omega = 1.064$. The frequency spectrum of the mode $k = 0.1125$, $n = 3$ in Fig.(14a) is given in Fig.(14b), which shows a peak at $\omega = 0.5369$, corresponding to a phase velocity $\omega / k = 4.78$. The frequency spectrum of the mode $k = 0.15$, $n = 4$ in Fig.(15a) is given in Fig.(15b), which shows a peak at $\omega = 0.719$, corresponding to a phase velocity $\omega / k = 4.793$. The frequency spectrum of the mode $k = 0.1875$, $n = 5$ in Fig.(16a) is given in Fig.(16b), which shows a peak at $\omega = 0.901$, corresponding to a phase velocity $\omega / k = 4.805$. The frequency spectrum of the mode $k = 0.225$, $n = 6$ in Fig.(17a) is given in Fig.(17b), which shows a peak at $\omega = 1.0833$, corresponding to a phase velocity $\omega / k = 4.814$. The frequency spectrum of the mode $k = 0.2625$, $n = 7$ in Fig.(18a) is given in Fig.(18b), which shows a peak at $\omega = 1.0546$, and at $\omega = 1.256$, whose phase velocities are $\omega / k = 3.63$ and $\omega / k = 4.784$ respectively, corresponding to the two inflexion points we see in Fig.(11a) around $\upsilon \approx 3.63$ and $\upsilon \approx 4.8$. The frequency spectrum of the mode $k = 0.3$, $n = 8$ in Fig.(19a) is given in Fig.(19b) during the growth of the mode from $t_1 = 100$ to $t_2 = 755$, and in Fig.(19c) at the end from $t_1 = 2344$ to $t_2 = 3000$. During the first phase of the evolution of the mode in Fig.(19b) the dominant peak is at $\omega = 1.0258$ (reaching a peak of about 500), and other peaks are seen at $\omega = 0.7382$, 1.112, 1.313, 1.7928. For the steady state spectrum in Fig.(19c), the two dominant peaks are at $\omega = 1.1025$ and $\omega = 1.438$, whose phase velocities ω / k are respectively at 3.675 and 4.793, corresponding to the two inflexion points we see in Fig.(11a). We present in Figs.(20-22) the time evolution of the modes with $k = 0.3375$, $n = 9$, $k = 0.45$, $n = 12$ and $k = 0.6$, $n = 16$ (this last one is the harmonic of the mode $n = 8$ in Fig.(19)).

Figs.(23a,b) and Fig.(24) show respectively the electric field plot, the potential plot and the electron density plot at t=2980. Note the rapid variation of the electric field plot at the position of the hole in the phase-space in Fig.(7o), and the corresponding peak in the potential in Fig.(23b). Note the cavity-like structure at the position of the phase-space hole in the electron density plot in Fig.(24). The ions remained essentially immobile, and showed some effects during the evolution of the system, immobilizing a very small oscillation which



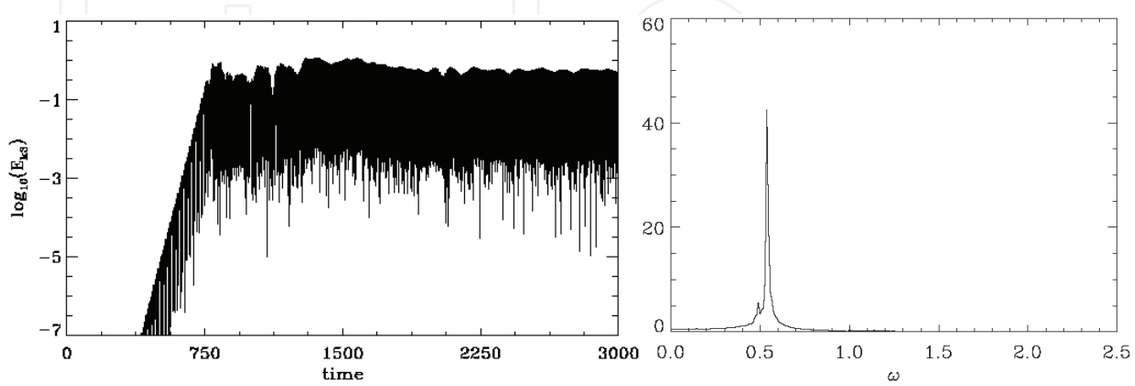
(a) (b)

Fig.12. (a) Time evolution of the Fourier mode k=0.0375
(b) Spectrum of the Fourier mode k=0.0375



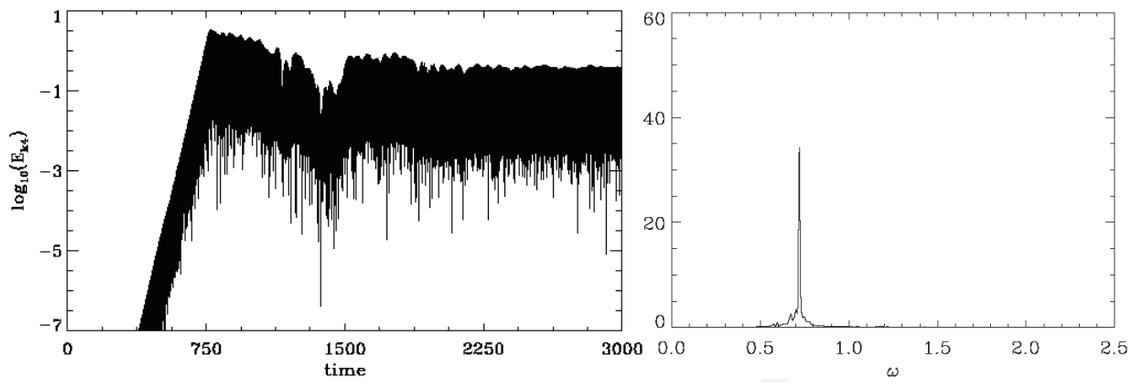
(a) (b)

Fig. 13. (a) Time evolution of the Fourier mode k=0.075
(b) Spectrum of the Fourier mode k=0.075



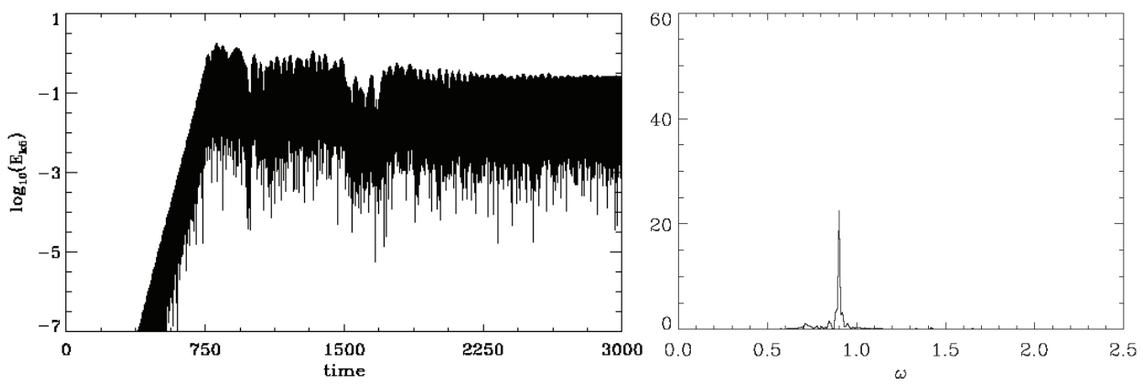
(a) (b)

Fig.14. (a) Time evolution of the Fourier mode with k=0.1125
(b) Spectrum of the Fourier mode k=0.112



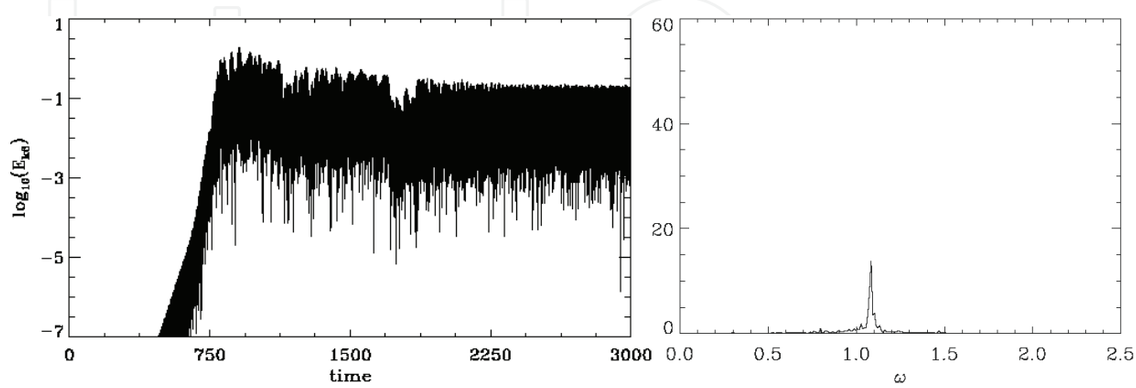
(a) (b)

Fig. 15. (a) Time evolution of the Fourier mode with k=0.15
(b) Spectrum of the Fourier mode k=0.15



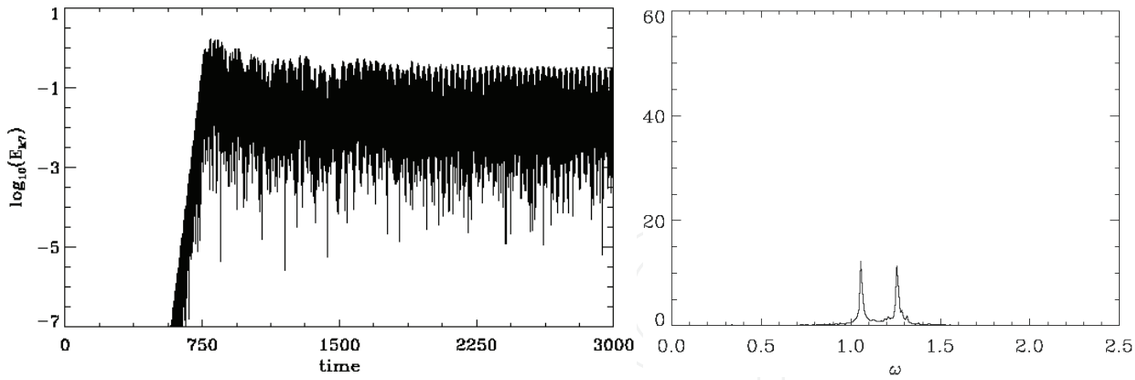
(a) (b)

Fig. 16. (a) Time evolution of the Fourier mode with k=0.1875,
(b) Spectrum of the Fourier mode k=0.1875



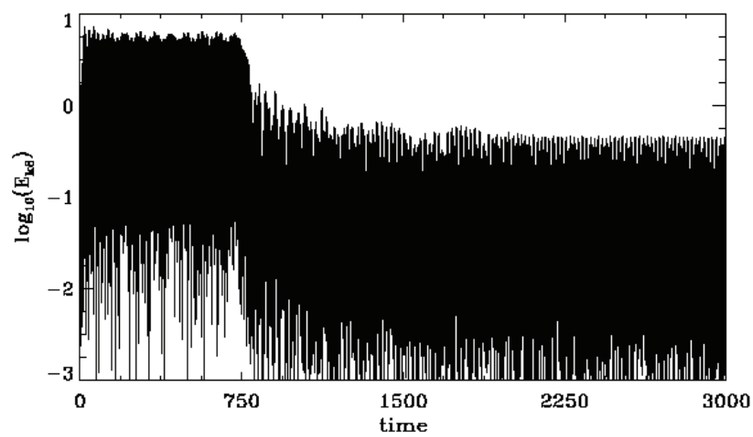
(a) (b)

Fig. 17. (a) Time evolution of the Fourier mode with k=0.225,
(b) Spectrum of the Fourier mode k=0.225

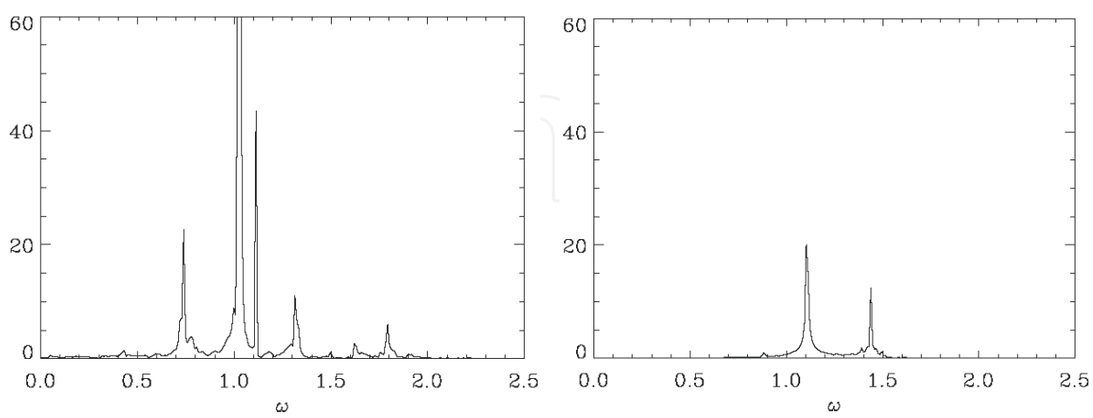


(a) (b)

Fig. 18. (a) Time evolution of the Fourier mode with k=0.2625,
(b) Spectrum of the Fourier mode k=0.2625



(a)



(b) (c)

Fig. 19. (a) Time evolution of the Fourier mode with k=0.3,
(b) Spectrum of the Fourier mode k=0.3 (from t=100. to t=755.36),
(c) Spectrum of the Fourier mode k=0.3 (from t=2344 to t=3000)

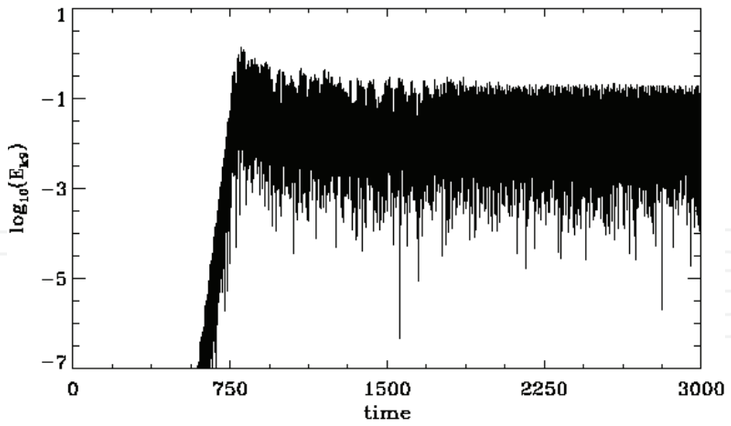


Fig. 20. Time evolution of the Fourier mode with k=0.3375

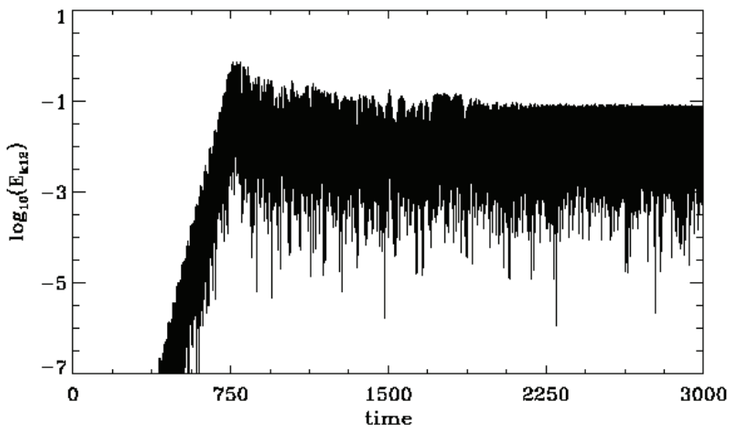


Fig. 21. Time evolution of the Fourier mode with k=0.45

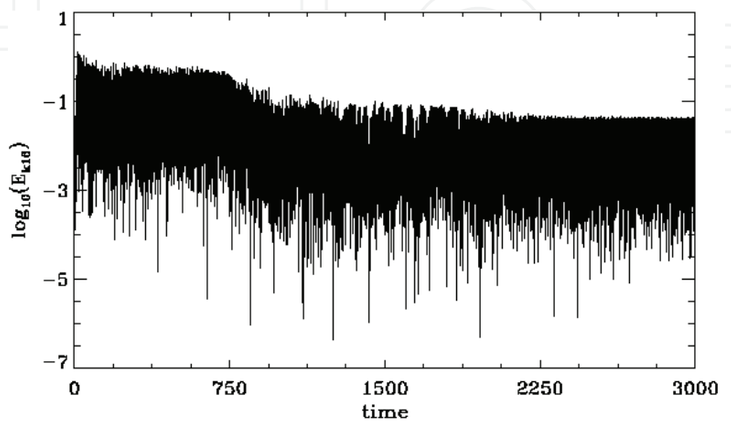
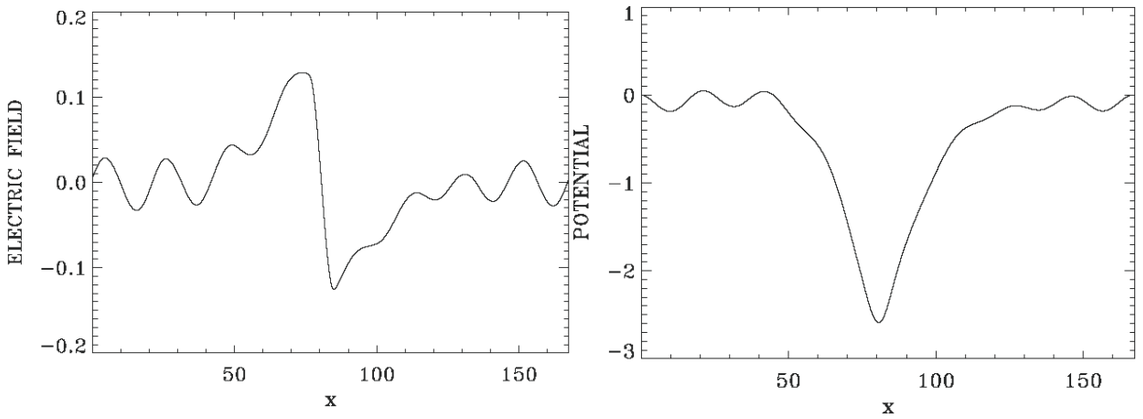


Fig. 22. Time evolution of the Fourier mode with k=0.6



(a) (b)

Fig. 23. (a) Electric field profile at *t*=2980 (b) Potential profile at *t*=2980.

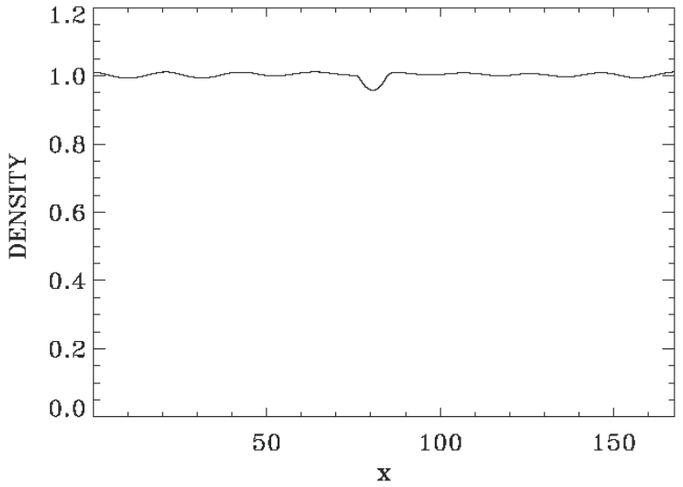


Fig. 24. Electron density profile at *t*=2980.

was persistent at the end of the simulation in the tail of the distribution function in Fig.(11a), without affecting the shape of the tail at all, especially what appeared to be the two inflexion points around $\upsilon \approx 3.7$ and $\upsilon \approx 4.8$. Also the evolution of the fusion of the two holes in Figs.(7h-7o) was much slower for the case of immobile ions, (lasting up to t=3000), with respect to what we see in the present results in Figs.(7h-7o) where the fusion is completed before *t*=2200.

4. Excitation of the modes n=7 and n=8 with k_a=0.2625 and k=0.3 respectively

We consider in this section the case when we excite initially two initially unstable modes with $k = n\frac{2\pi}{L} = 0.3$, $n = 8$, and $k_a = 0.2625$, $n = 7$. So the initial electron distribution function is given by:

$$f_e(x,\upsilon_e) = f(\upsilon_e)(1 + \varepsilon\cos(kx) + \varepsilon_a\cos(k_a x))) \tag{7}$$

$f_e(\upsilon_e)$ is defined in Eq.(4). We use $\varepsilon = \varepsilon_a = 0.04$. The linear solution for the frequency associated with the mode $k = 0.3$ is $\omega^2 \approx 1 + 3k^2$, or $\omega \approx 1.127$, with a phase velocity of the wave $\omega / k \approx 3.756$. The linear solution for the frequency associated with the mode $k_a = 0.2625$ is 1.0985, with a phase velocity of the wave $1.0985 / 0.2625 = 4.184$. Both phase velocities fall on the positive slope of the bump-on-tail distribution function, as can be verified from Fig.(3). So both initially excited modes are unstable.

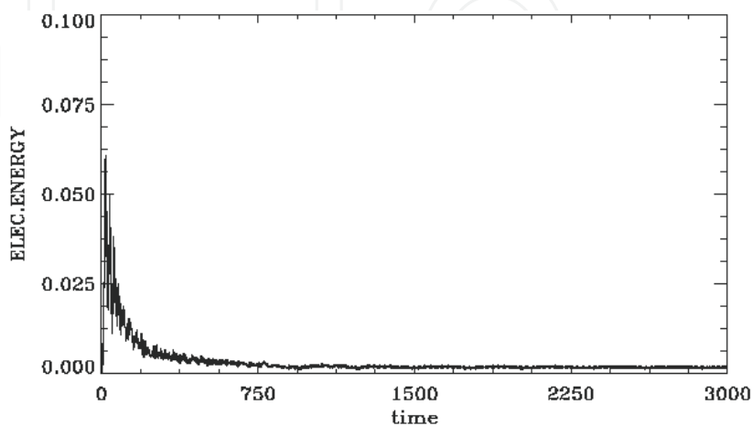


Fig. 25. Time evolution of the electric field energy.

Fig.(25) presents the time evolution of the electric field energy, which contrasts with what is presented in Fig.(1). Fig.(25) shows a rapid growth in the linear phase, followed by a rapid decay of the electric field energy. The spatially averaged electron distribution function shows very rapidly the formation of an elongated tail. We present in Fig.(26a) the spatially averaged electron distribution function at $t = 400$, and in Fig.(26b) we concentrate on the region of the tail, where the plot on a logarithmic scale show at this stage of the evolution a slowly decaying distribution function.

We present in Fig.(27a-o) the evolution of the phase-space. From the early beginning, the vortices formed due to the trapping of particles are unstable. Energy flows to the longest

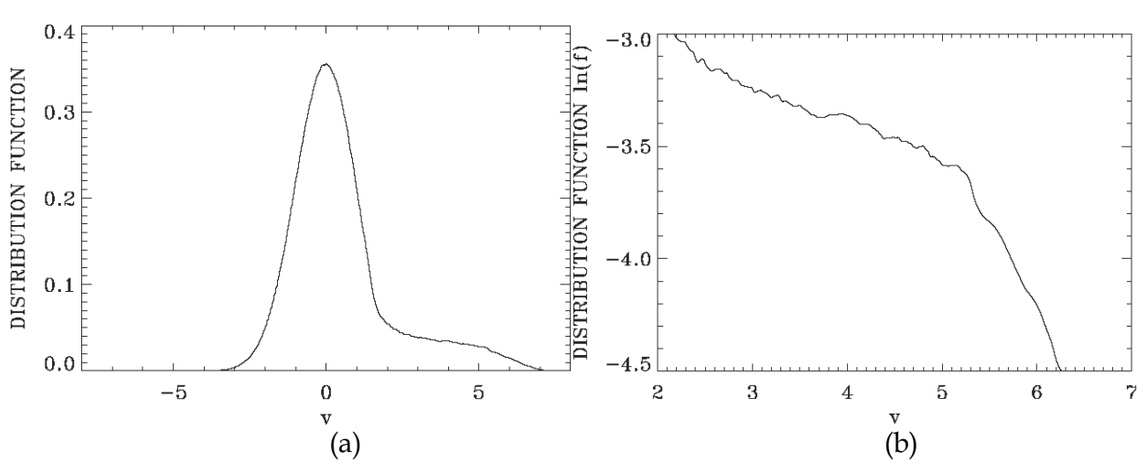


Fig. 26. (a) Spatially averaged distribution function at $t = 400$,
(b) Same as Fig.(26a), concentrating on the tail region.

wavelengths, which is characteristic of 2D systems (Knorr,1977). During this evolution the center of the vorticies is moving to higher velocities. In Fig.(27d) at $t = 600$, we have two holes left, which then start merging together. In Fig.(27f) at $t = 760$, one of the two vortices starts occupying a satellite position around the other, and then starts spiralling around it, leaving in the long run a single vortex (the evolution at this stage is similar to what has been presented in the previous section in Figs.(7i-n)). At $t = 3000$ in Fig.(27o), we show the final single vortex, centered around ≈ 5.05. Note also in Fig.(27g) the presence of a small vortex along the upper boundary. In Figs.(27i-j) this small vortex moves closer to the big vortex, and then in Figs.(27k-m) it goes spiraling around the big vortex. Fig.(28) is a 3D plot of the hole presented in Fig.(27o). Note the associated cavity structure in the bulk which travels as a solitary like structure in the phase-space. In Fig.(29a) we show the spatially averaged electron distribution function at $t = 3000$, and in Fig.(29b) we present on a logarithmic scale the same curve, concentrating in the tail region.

Although the initial evolution of the system is totally different from what we see in the previous section, the final result in Fig.(27o) showing a hole in the phase-space is close to what has been presented in the previous section. There are, however, important differences between the results in Fig.(27o) and the results in Fig.(7o). The hole in Fig.(27o) is centered at a higher velocity than the hole in Fig.(7o). We observe also the plot of the tail in Fig.(29b) being shifted to higher velocities than the plot of the tail in Fig.(11a). Indeed, in Fig.(29b) the inflexion points are around $\upsilon \approx 4.05$ and around $\upsilon \approx 5.05$, while in Fig.(11a) the inflexion points are around $\upsilon \approx 3.7$ and $\upsilon \approx 4.8$. We present in Fig.(30a) the same electron distribution function as in Fig.(29a) at $t = 3000$, concentrating at the top of the distribution function. There is a deformation at the top which appears more important than the one at the top of Fig.(11d). Also the contour plot in Fig.(30b) at the top of the electron distribution function shows a rich collection of small vortices, more important than what we observe in Fig.(11d). Fig.(31a) and Fig.(31b) present the electric field and the electron density profiles at $t = 3000$. See in Fig.(31a) the rapid variation of the electric field from a positive to negative value at the position of the phase-space hole in Fig.(27o). See in Fig.(31b) the cavity structure in the density plot at the position of the phase-space hole. The ions showed essentially very small variation, and a flat density profile. However, this small variation provides the stable profile in Fig.(29). In the absence of the ions, the profile in Fig.(29b) would show a very small oscillation.

Figs.(32-44) present the Fourier modes and their frequency spectra. We note from these figures that the initial growth of the longest wavelengths during the process of inverse cascade is higher with respect to what we see in Figs(12a-18a) for instance. There is a modulation in the asymptotic state which is more important in Figs.(32-44). The frequency spectrum is calculated by transforming the different Fourier modes in the last part of the simulation from $t_1 = 2344$ to $t_2 = 3000$. The frequency spectrum of the mode with $k = 0.0375$, $n = 1$ in Fig.(32a) shows a peak at $\omega = 0.19175$. The phase velocity of this mode $\omega / k = 5.11$ .Two other small peaks appear in Fig.(32b) at $\omega = 0.9875$ and 1.0258. The frequency spectrum of the mode with $k = 0.075$, $n = 2$ in Fig.(33a) has a peak at $\omega = 0.374$, corresponding to a phase velocity ≈ 5. It has also two small peaks at a frequency $\omega = 0.9875$ and 1.0738. The frequency spectrum of the mode with $k = 0.1125$, $n = 3$ in Fig.(34a) has a peak at a frequency $\omega = 0.5656$ in Fig.(34b), corresponding to a phase velocity ≈ 5.03. It has also a small peak at $\omega = 0.997$. The frequency spectrum of the mode with $k = 0.15$, $n = 4$ in

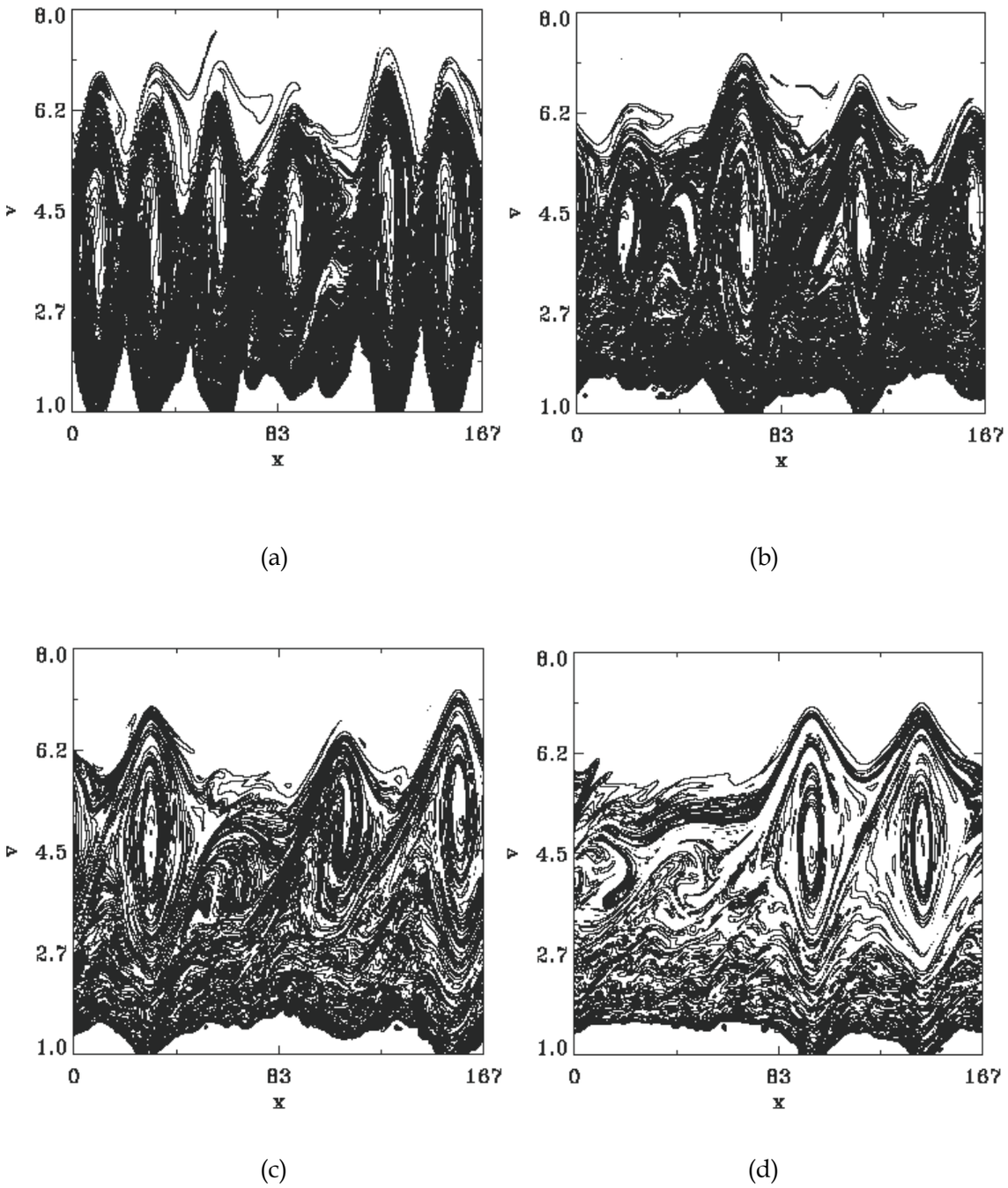
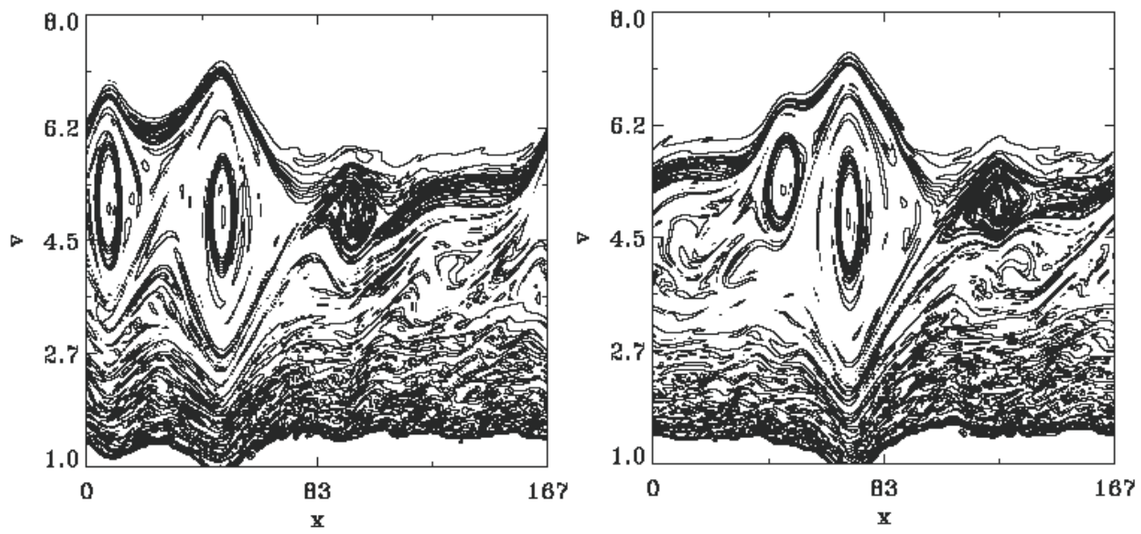
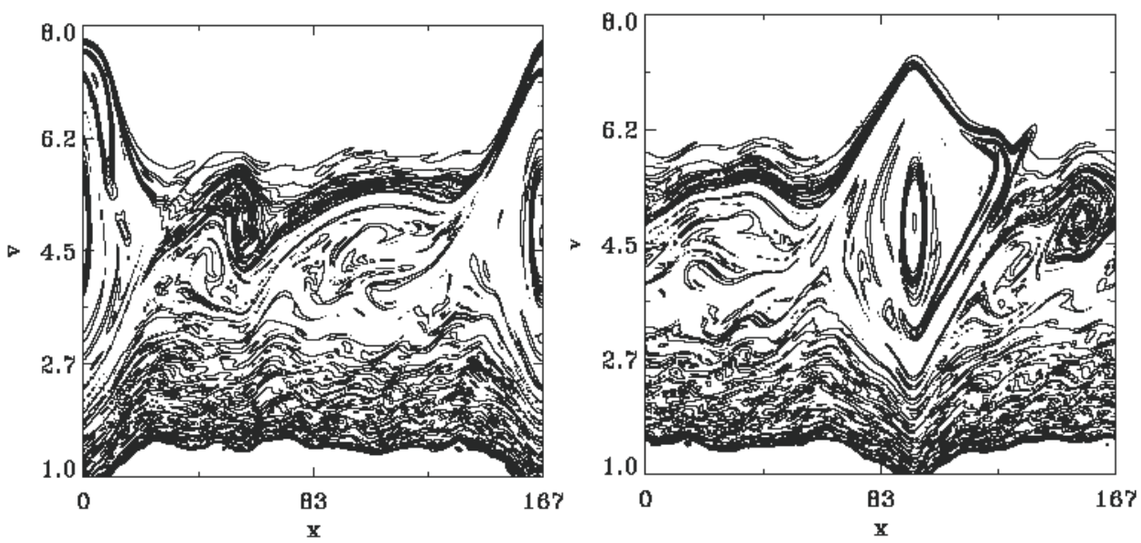


Fig. 27. (a) Contour plot of the distribution function, $t = 60$
(b) Contour plot of the distribution function, $t = 200$
(c) Contour plot of the distribution function, $t = 400$
(d) Contour plot of the distribution function, $t = 600$

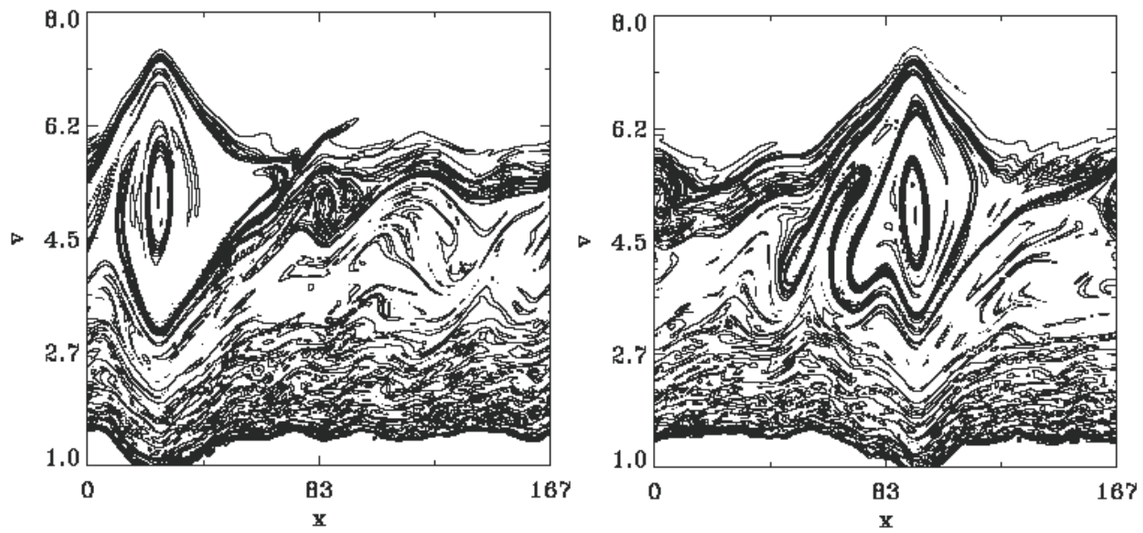


(e) (f)

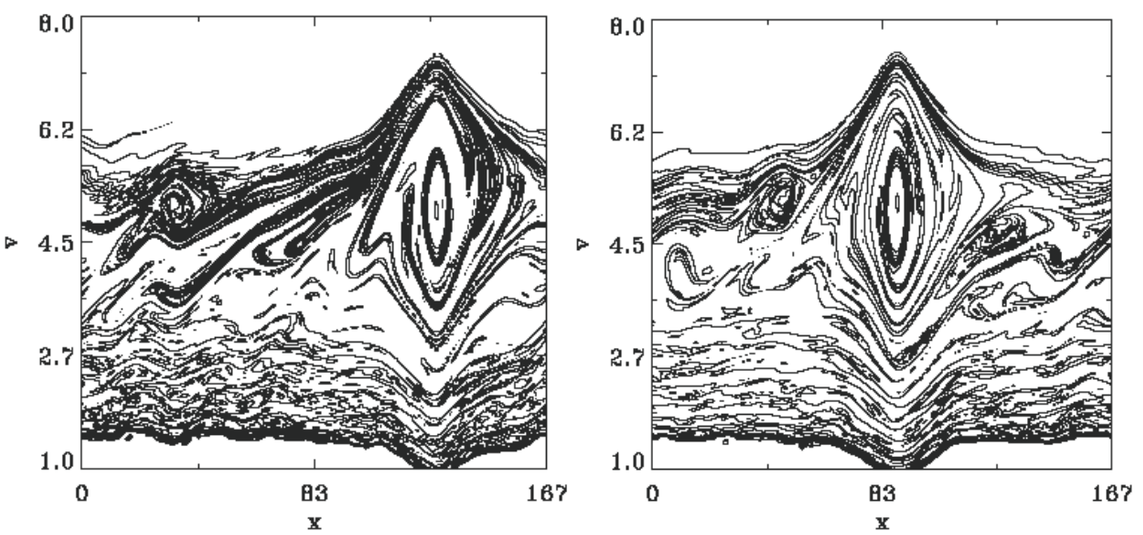


(g) (h)

Fig. 27. (e) Contour plot of the distribution function, $t = 720$
(f) Contour plot of the distribution function, $t = 760$
(g) Contour plot of the distribution function, $t = 780$
(h) Contour plot of the distribution function, $t = 800$

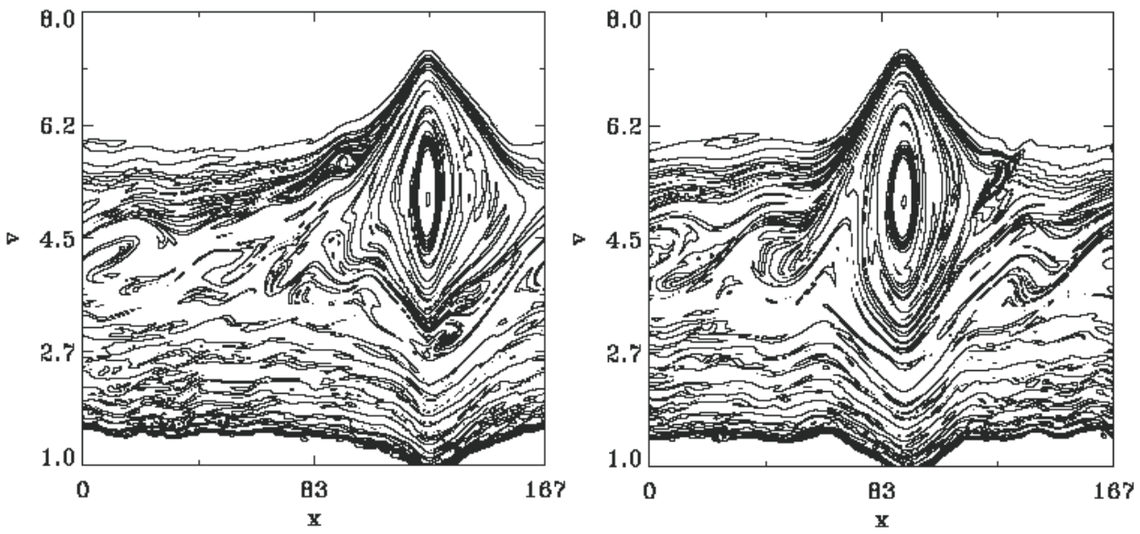


(i) (j)

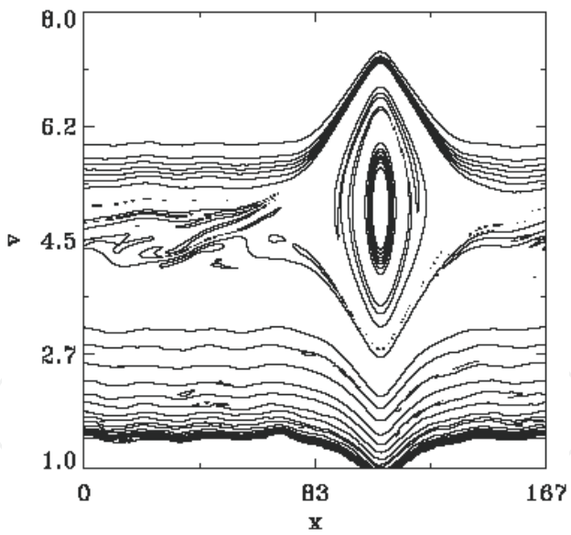


(k) (l)

Fig. 27. (i) Contour plot of the distribution function, $t = 820$
(j) Contour plot of the distribution function, $t = 900$
(k) Contour plot of the distribution function, $t = 940$
(l) Contour plot of the distribution function, $t = 1200$



(m) (n)



(o)

Fig. 27. (m) Contour plot of the distribution function, $t = 1240$
(n) Contour plot of the distribution function, $t = 1300$
(o) Contour plot of the distribution function, $t = 3000$

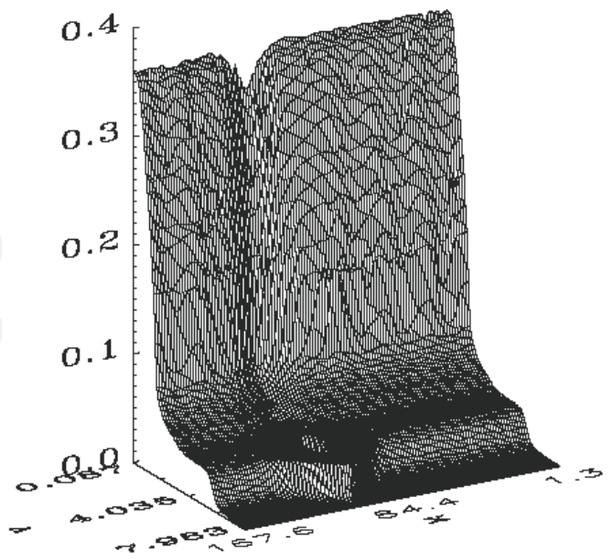
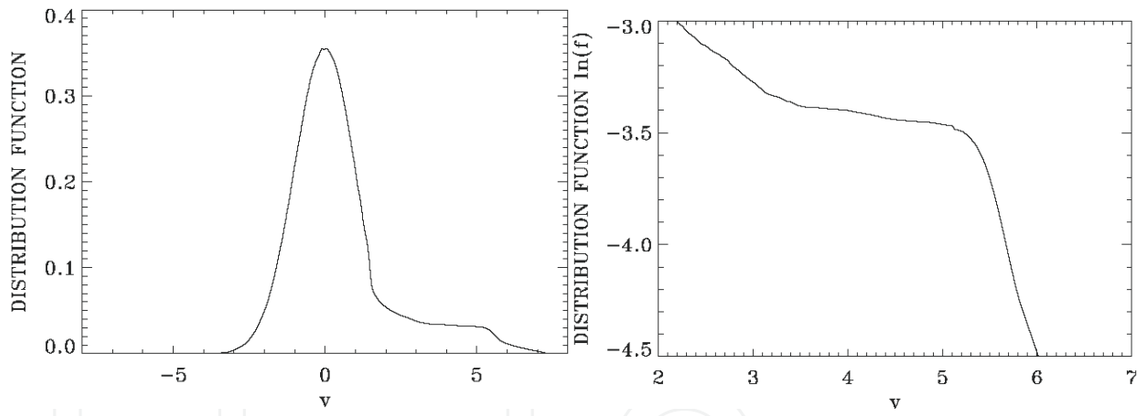


Fig. 28. Same as Fig.(27o), 3D plot at $t = 3000$



(a) (b)

Fig. 29. (a) Spatially averaged distribution function, $t = 3000$
(b) Same as Fig.(29a), concentrating on the tail region.

Fig.(35a) has a peak at a frequency $\omega = 0.7574$ in Fig.(35b), corresponding to a phase velocity ≈ 5.05 . The frequency spectrum of the mode with $k = 0.1875$, $n = 5$ in Fig.(36a) has a peak at $\omega = 0.944$ in Fig.(36b), corresponding to a phase velocity ≈ 5.034 . The frequency spectrum of the mode with $k = 0.225$, $n = 6$ in Fig.(37a) has a peak at a frequency $\omega = 1.1313$ in Fig.(37b), corresponding to a phase velocity ≈ 5.028 . It has also peaks at $\omega = 1.0258$ and 1.256 , which underline the modulation of the mode in Fig.(37a). All the previous modes have a phase velocity ≈ 5.05 , which corresponds to the inflexion point of zero slope we see in Fig.(29b). So the dominant frequencies of oscillation of these modes seem to adjust themselves in such a way that the phase velocities of these modes would correspond to the

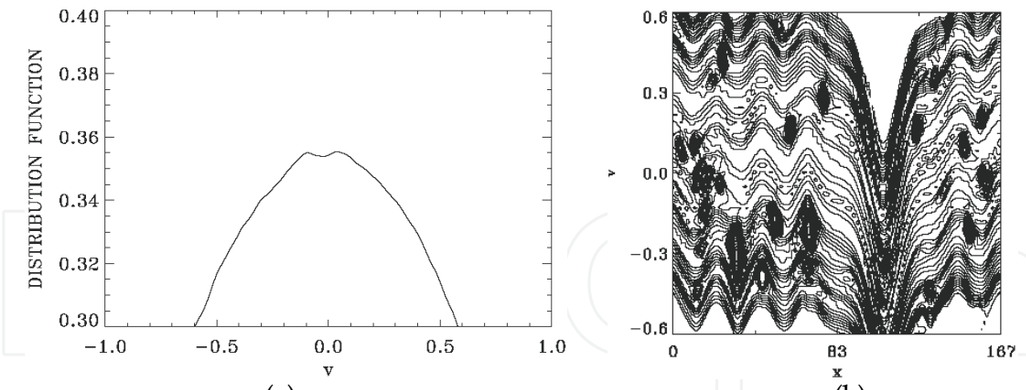


Fig. 30. (a) Same as Fig.(29a) (concentrates on the top)
(b) Contour plot for the distribution in Fig.(30a)

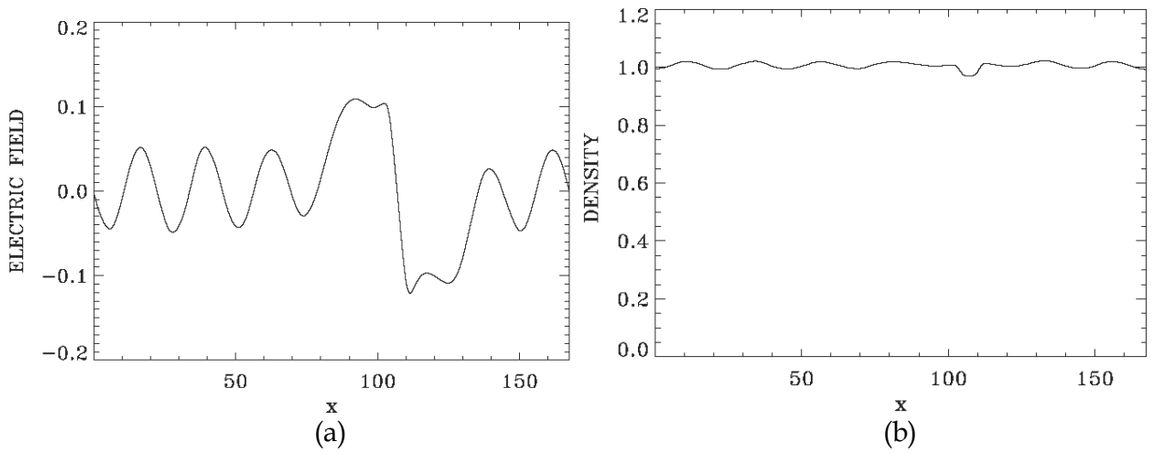


Fig. 31. (a) Electric field profile at $t = 3000$,
(b) Electron density profile at $t = 3000$

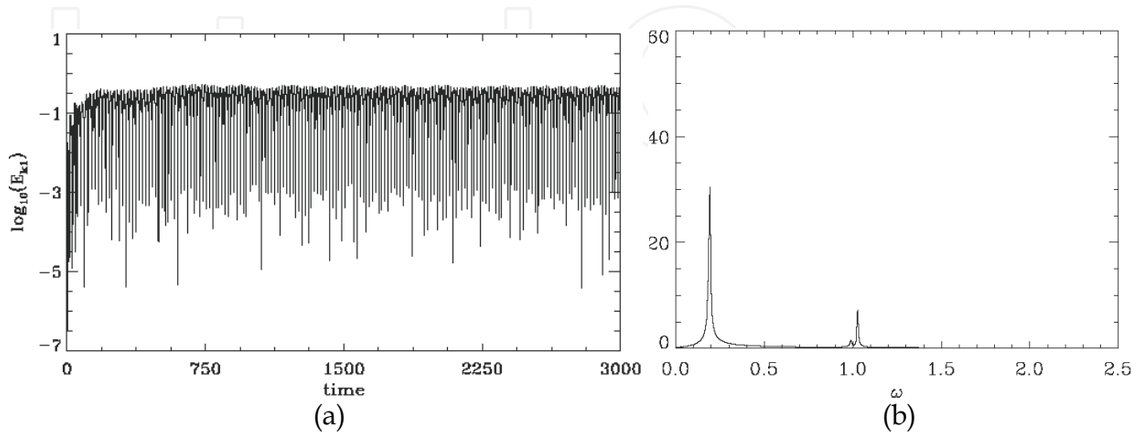
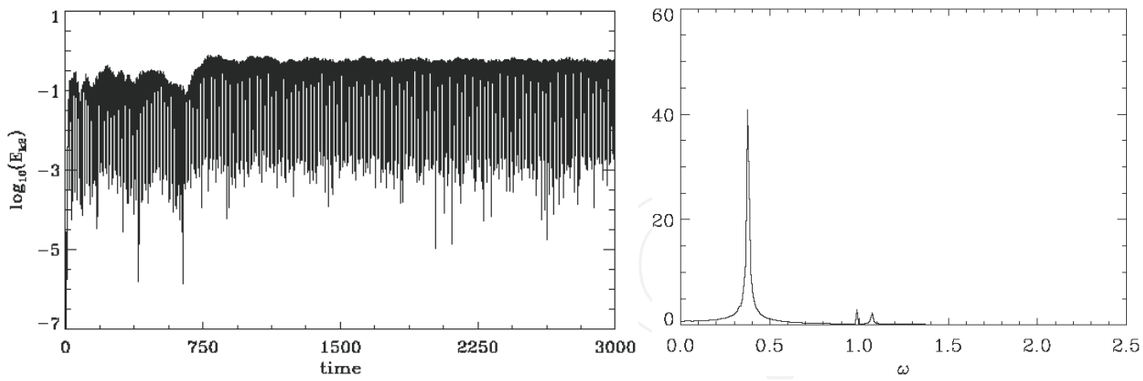
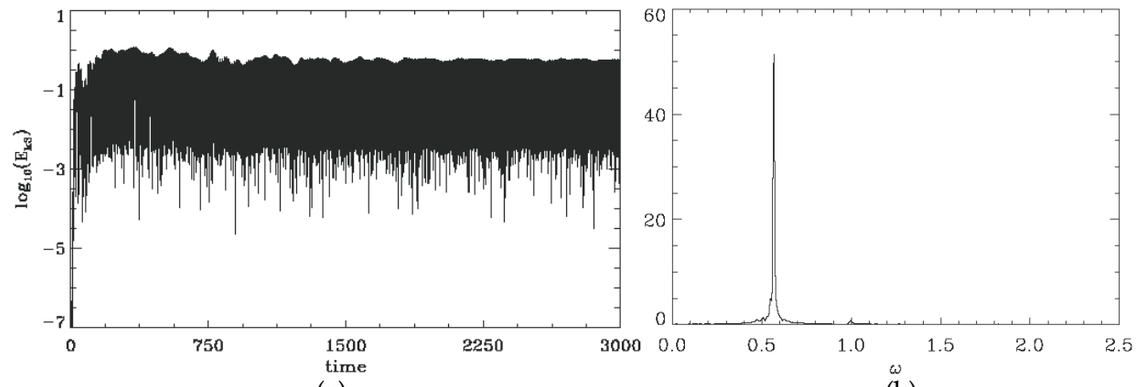


Fig. 32. (a) Time evolution of the Fourier mode k=0.0375,
(b) Spectrum of the Fourier mode k=0.0375



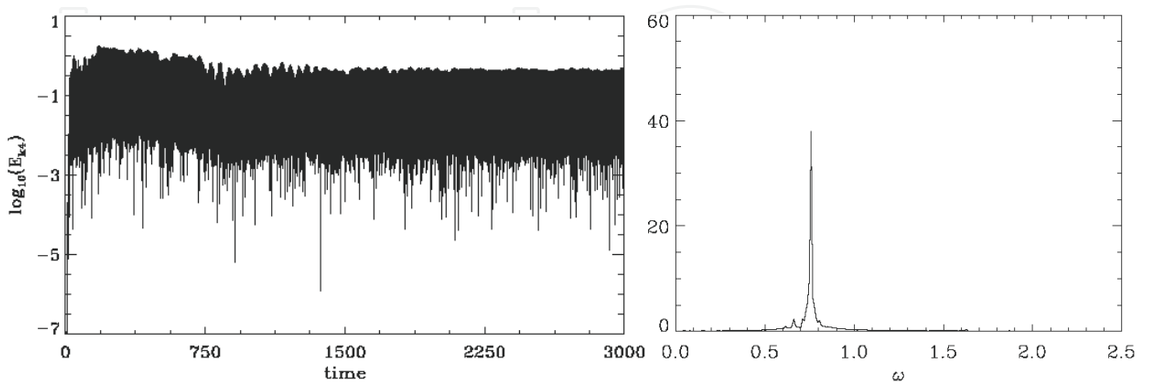
(a) (b)

Fig. 33. (a) Time evolution of the Fourier mode k=0.075,
(b) Spectrum of the Fourier mode k=0.075



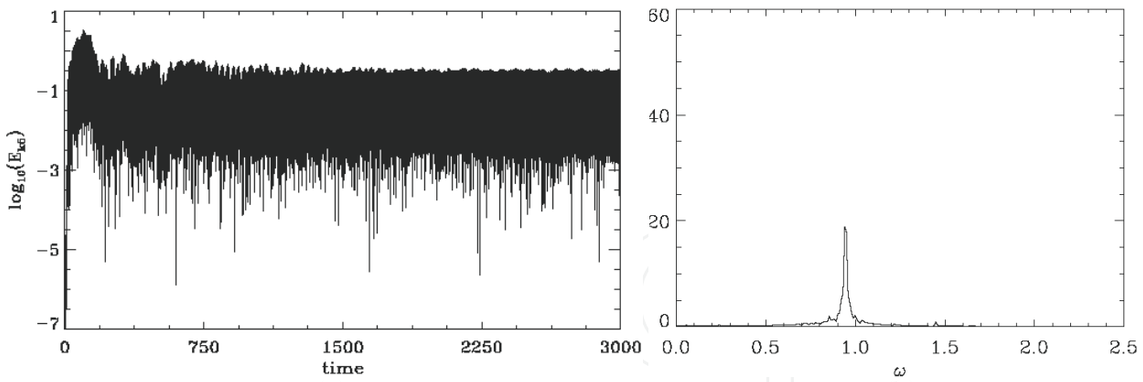
(a) (b)

Fig. 34. (a) Time evolution of the Fourier mode k=0.1125,
(b) Spectrum of the Fourier mode k=0.1125



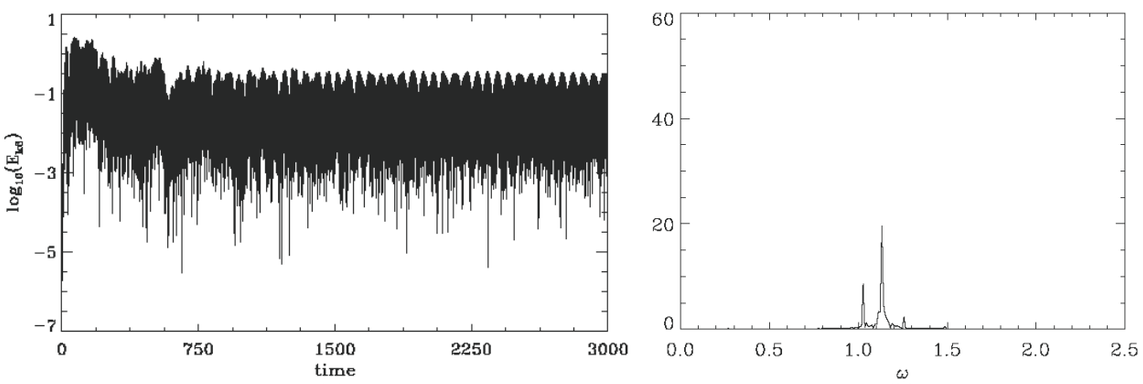
(a) (b)

Fig. 35. (a) Time evolution of the Fourier mode k=0.15
(b) Spectrum of the Fourier mode k=0.15



(a) (b)

Fig. 36. (a) Time evolution of the Fourier mode k=0.1875,
(b) Spectrum of the Fourier mode k=0.1875



(a) (b)

Fig. 37. (a) Time evolution of the Fourier mode k=0.225,
(b) Spectrum of the Fourier mode k=0.225

inflexion point established by the trapped population, to allow the mode to oscillate at a constant amplitude. The mode $n=7$ in Fig.(38a) is one of the two initially unstable modes. Fig.(38b) gives the frequency spectrum of this mode in the initial phase of the evolution from $t_1=100$ to $t_2=755$, showing a broad spectrum with two dominant peaks at $\omega=1.064$ and 1.227. In the steady state at the end of the simulation, the frequency spectrum of the mode with $k=0.2625$, $n=7$ has a dominant peak at a frequency $\omega=1.0642$ and a peak at $\omega=1.323$ in Fig.(38c), corresponding to a phase velocity respectively of ≈ 4.05 and ≈ 5.04. These two velocities correspond to the two inflexion points of zero slope we see in Fig.(29b). The mode $n=8$ in Fig.(39a) is also one of the two initially unstable modes. Fig.(39b) gives the frequency spectrum of this mode in the initial phase of the evolution, from $t_1=100$ to $t_2=755$, showing a broad spectrum with two dominant peaks at $\omega=1.112$ and 1.428. In the steady state at the end of the simulation, the frequency spectrum of the mode with $k=0.3$, $n=8$ has a peak at a frequency $\omega=1.112$ and a peak at a frequency 1.5148 in Fig.(39c), corresponding to a phase velocity respectively of ≈ 3.7 and ≈ 5.05. This second velocity corresponds to the inflexion point we see in Fig.(29b). The mode at $\omega=1.112$ would correspond to a coupling between the modes $n=1$ and $n=7$ (for the

wavenumbers $0.0375 + 0.2625 = 0.3$, and for the frequencies $0.182 + 1.0642 = 1.246$). The frequency spectrum of the mode with $k = 0.3375$, $n = 9$ in Fig.(40a) has a peak at a frequency $\omega = 1.6969$ in Fig.(40b), corresponding to a phase velocity ≈ 5.028, which corresponds to the inflexion point we see in Fig.(29b). Two small frequency peaks are also appearing at 0.6903 and 0.9204 and are also present in Fig.(40b). The frequency spectrum of the mode with $k = 0.375$, $n = 10$ in Fig.(41a) has a peak at a frequency $\omega = 1.8887$ in Fig.(41b), corresponding to a phase velocity ≈ 5.036, which corresponds to the inflexion point we see in Fig.(29b). The frequency spectrum of the mode with $k = 0.45$, $n = 12$ in Fig.(42a) has a peak at a frequency $\omega = 2.26262$ in Fig.(42b), corresponding to a phase velocity ≈ 5.028, which corresponds to the inflexion point we see in Fig.(29b). Finally Fig.(43) shows the time evolution of the mode with $k = 0.525$, $n = 14$ (the harmonic of the mode $n = 7$ in Fig.(38a)), and Fig.(44) shows the time evolution of the mode with $k = 0.6$, $n = 16$ (the harmonic of the mode $n = 8$ in Fig.(39a)).

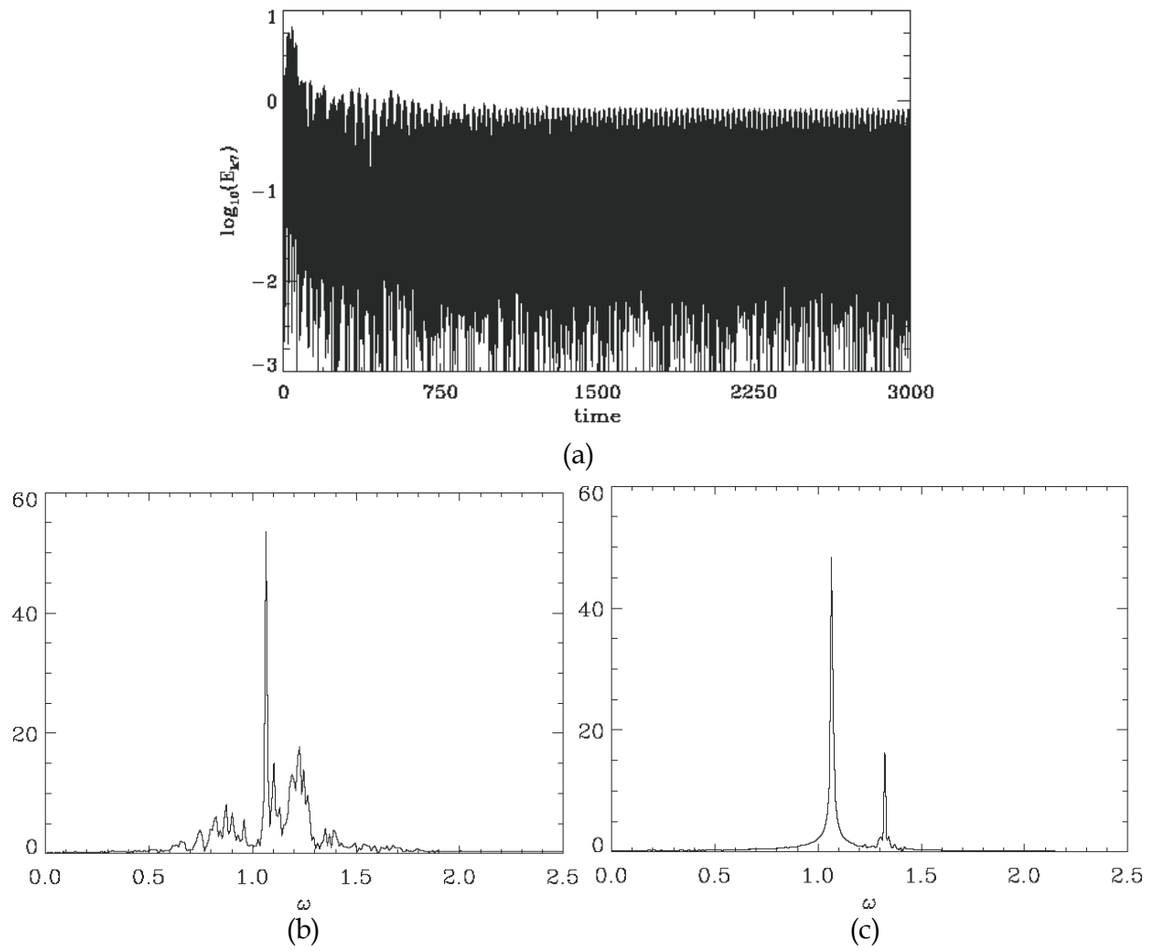


Fig. 38. (a) Time evolution of the Fourier mode k=0.2625,
(b) Spectrum of the Fourier mode k=0.2625 (from $t_1 = 100$ to $t_2 = 755$),
(c) Spectrum of the Fourier mode k=0.2625 (from $t_1 = 2344$ to $t_2 = 3000$)

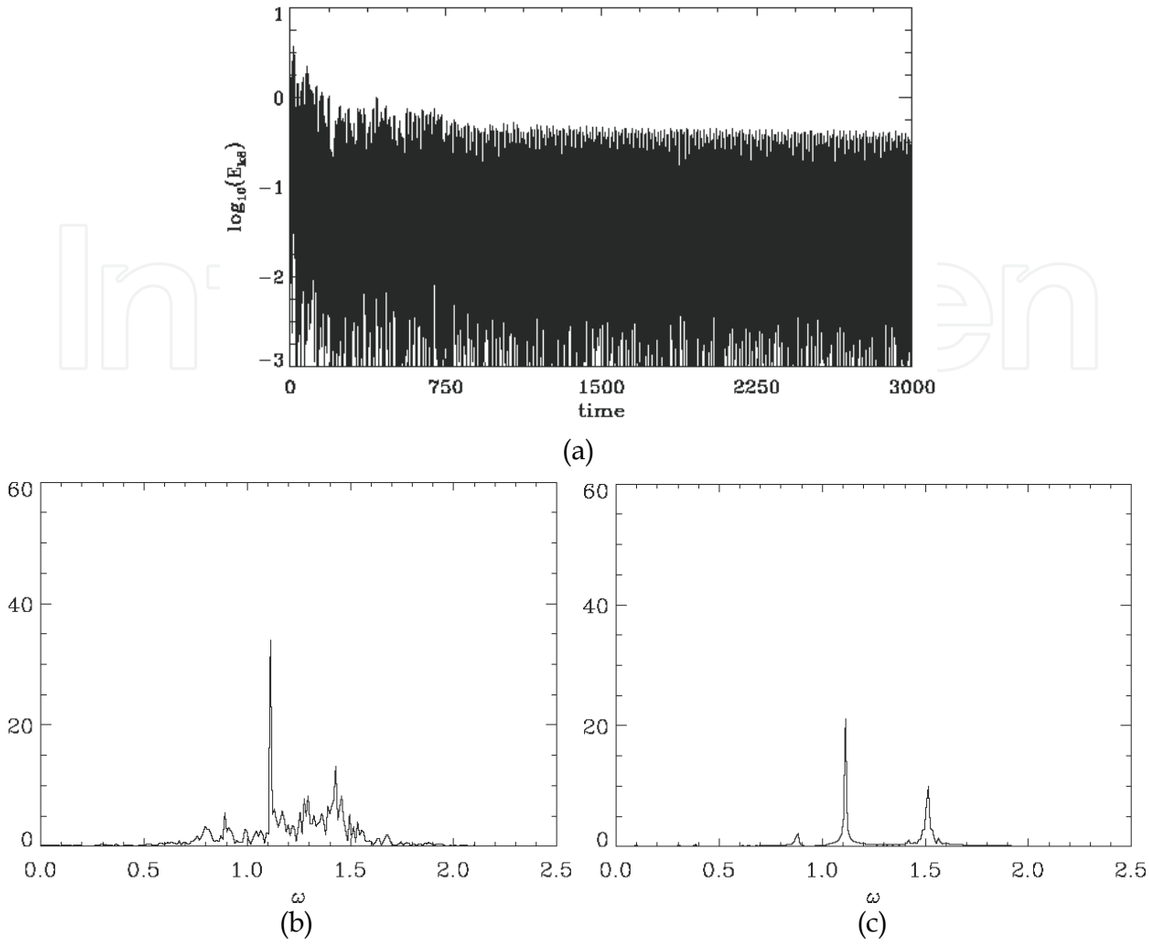


Fig. 39. (a) Time evolution of the Fourier mode k=0.3
(b) Spectrum of the Fourier mode k=0.3 (from $t_1 = 100$ to $t_2 = 755$
(c) Spectrum of the Fourier mode k=0.3 (from $t_1 = 2344$ to $t_2 = 3000$)

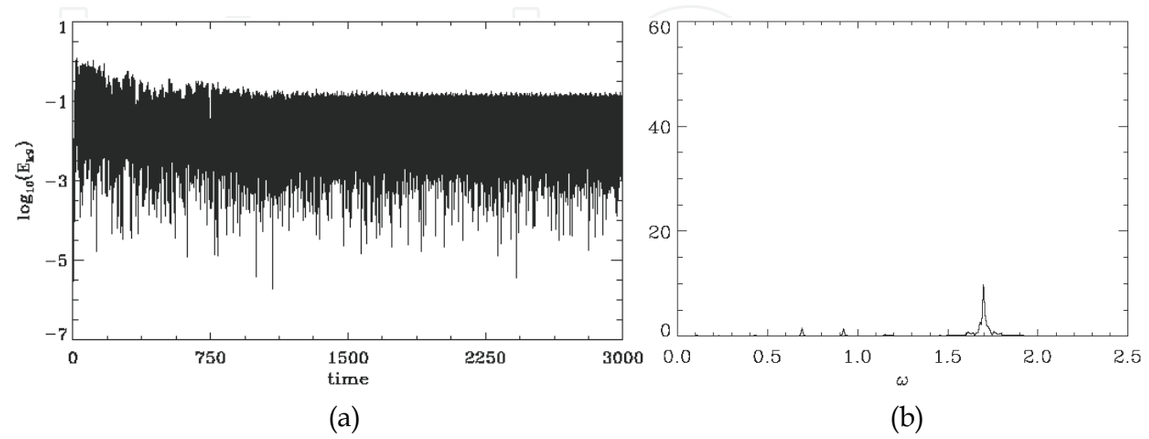
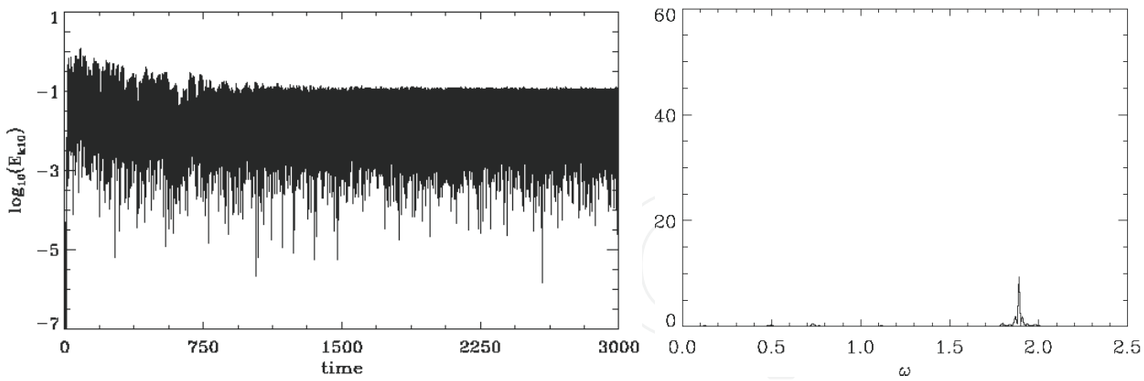
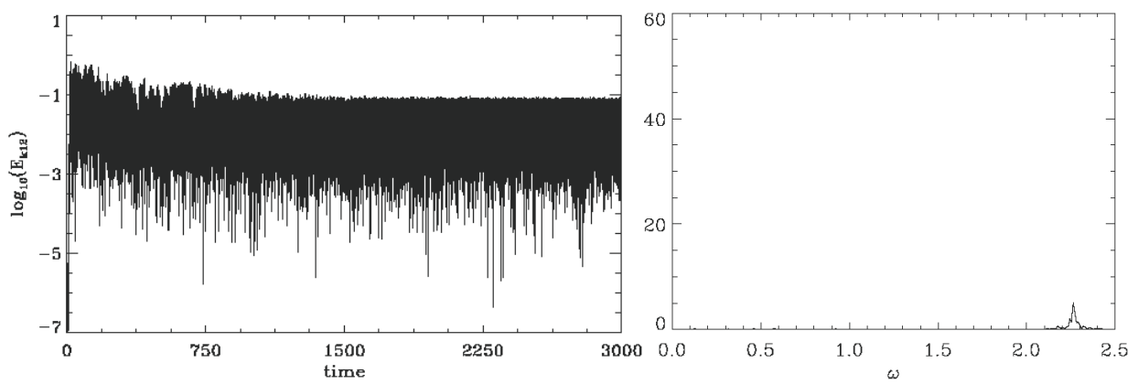


Fig. 40. (a) Time evolution of the Fourier mode k=0.3375,
(b) Spectrum of the Fourier mode k=0.3375



(a) (b)

Fig. 41. (a) Time evolution of the Fourier mode k=0.375,
(b) Spectrum of the Fourier mode k=0.375



(a) (b)

Fig. 42. (a) Time evolution of the Fourier mode k=0.45,
(b) Spectrum of the Fourier mode k=0.45

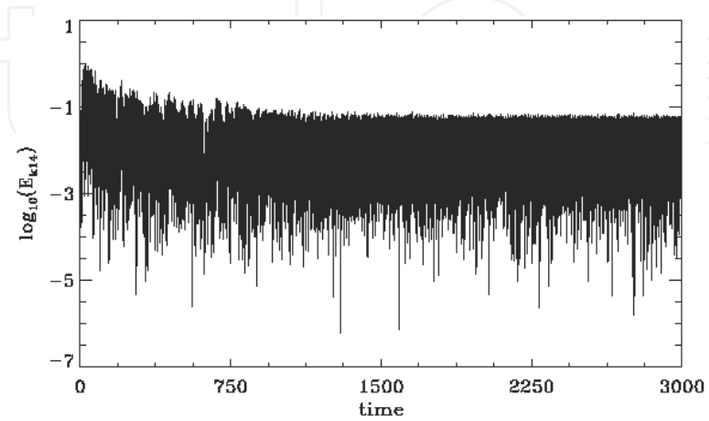


Fig. 43. Time evolution of the Fourier mode k=0.525

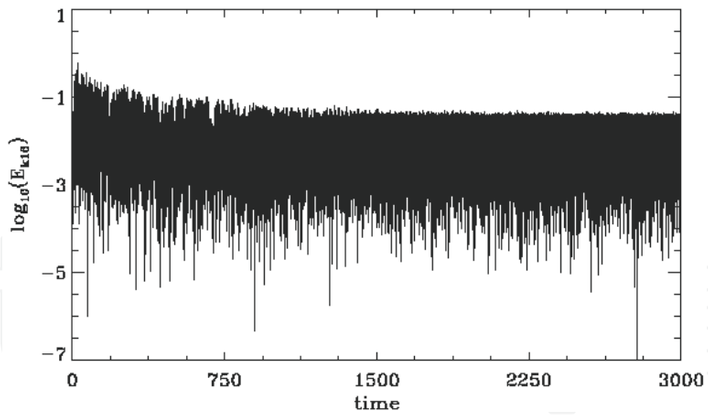


Fig. 44. Time evolution of the Fourier mode k=0.6

5. Conclusion

In the present Chapter, we have presented a study for the long-time evolution of the Vlasov-Poisson system for the case when the beam density is about 10% of the total density, which provides a vigorous beam-plasma interaction and an important wave-particle interaction, and which results in important trapped particles effects. A warm beam is considered, and the length of the system L is larger than the initially unstable wavelength λ, which allows the growth of sidebands. A fine resolution grid in the phase-space and a small time-step are used to follow the nonlinear dynamics of the trapped particles as accurately as possible. Numerical grid size effects and small time-steps can have important consequences on the number and distribution of the trapped particles, on the dynamical transitions of the Vlasov-Poisson system, and on kinetic microscopic processes such as the chaotic trajectories which appear in the resonance region at the separatrix of the vortex structures where particles can make transitions from trapped to untrapped and retrapped motion. The importance of the microscopic processes for their possible consequences on the macroscopic large scale dynamics have been also stressed in several publications (Califano *et al*., 2000, Shoucri, 2010).

Initial conditions can also have important consequences on the microscopic processes, on the dynamical transitions of the Vlasov-Poisson system, and their possible effects on the large scale dynamics. Two cases have been considered in this Chapter. A case where a single initially unstable mode is excited, and a case where two initially unstable modes are excited. In the first case the evolution of the electric energy shows initially the classical behaviour of the growth of the initially unstable wave, followed by the saturation of the instability and the formation of BGK vortices in the phase-space, and the electric field is oscillating around a constant amplitude, modulated by the trapped particles oscillation. The subsequent evolution is dominated by a fusion of the vortices and by an inverse cascade where energy flows to the longest wavelengths available in the system, a process characteristic of 2D systems (Knorr, 1977). In the second case where two initially unstable waves are excited, the initial growth of the electric energy is followed by a rapid decay. This is accompanied by the formation of unstable vortex structures. In both cases the system evolves towards the formation of a single hole in the phase-space, where the trapped particles are accelerated to high velocities. The electron density plot shows the formation of a cavity like structure corresponding to the hole in the phase-space (Fig.(24) and (31b)).

Oscillation frequencies below the plasma frequency are associated with the longest wavelengths. The spatially averaged distribution functions show curves having a tail with a slowly decaying slope, and this slope takes the value of zero at the phase velocities of the dominant waves (see Fig.(11a) and (29b)). We note that for the second case in Fig.(29b), the acceleration of the particles in the tail is higher with respect to the first case in Fig.(11a). The low frequencies associated with the dominant longer wavelengths result in higher phase velocities of the different modes, which are accelerating trapped particles to higher velocities in the tail of the distribution function, with kinetic energies above the initial energy of the beam (see the recent work in Sircombe *et al*., 2006, 2008). The trapped accelerated population is adjusting in return in order to provide the distribution function with a zero slope at the phase velocities of the waves, allowing the different modes to oscillate at a constant amplitude (modulated by the oscillation of the trapped particles). The increase in the kinetic energy due to the particles acceleration is equivalent to the decrease in the electric energy we see in Fig.(1) and in Fig.(25).

The problem when several unstable modes are initially excited is certainly of interest. We note that when four initially unstable modes in a longer system were excited, the general evolution and the final results obtained were close to what we have presented in section 4 for the case of two unstable modes. Some additional results presented in Ghizzo *et al*. 1988, for this problem have shown a strong acceleration of particles in the case $n_b = 0.1$, in which case the tail particles are accelerated considerably to velocities higher than twice the initial beam velocity. The distribution function in this case takes the shape of a two-temperature Maxwellian distribution function with a high energy tail having a smooth negative slope. This result seems to agree with experimental observations from current drive experiments using an electron beam injected into the plasma (Advanced Concept Torus ACT-1 device), where it was observed that a significant fraction of the beam and background electrons are accelerated considerably beyond the initial beam velocity (Okuda *et al*., 1985). In none of the ACT-1 discharges is a distinctive feature of a plateau predicted from quasilinear theory apparent in the distribution function. The evolution of the waves amplitude in the results reported in Ghizzo *et al*., 1988, shows a rapid rise, followed by an abrupt collapse of the waves amplitude, the energy being delivered to the accelerated particles. When n_b is decreased, the acceleration of the particles is decreased, and when it is reduced to $n_b = 0.01$, a quasilinear plateau is formed and the waves amplitude saturate at a constant level. We note that when the simulations presented in sections 4 and 5 are repeated with $n_b = 0.01$, a quasilinear plateau is formed, without the acceleration we see in sections 4 and 5. Finally we point to the results obtained in Manfredi *et al*., 1996, with two spatial dimensions and a magnetic field, which shows in a bump-on-tail instability a rich variety of physics including also the acceleration of particles to high energies.

6. Acknowledgements

M. Shoucri is grateful to the Institut de Recherche d'Hydro-Québec (IREQ) computer center CASIR for computer time used to do the present work.

7. References

Berk, H.L., Roberts, K.V. (1967). Nonlinear study of Vlasov's equation for a special class of distribution functions. *Phys. Fluids* 10, 1595-1597

Bernstein, M., Greene, J.M., Kruskal, M.D. (1957). Exact nonlinear plasma oscillations. *Phys., Rev.* 108, 546-550

Bertrand, P., Ghizzo, A., Feix, M., Fijalkow, E., Mineau, P., Suh, N.D., Shoucri, M., (1988). Computer simulations of phase-space hole dynamics, In: *Nonlinear Phenomena in Vlasov Plasmas*, F. Doveil, (Ed.), p.109-125, Editions de Physique, Orsay.

Buchanan, M., Dorning, J. (1995). Nonlinear electrostatic waves in collisionless plasmas. *Phys. Rev. E* 52, 3015-3033

Califano, F., Lantano, M. (1999). Vlasov-Poisson simulations of strong wave-plasma interaction in condition of relevance for radio frequency plasma heating. *Phys. Rev. Lett.* 1999, 83, 96-99

Califano, F., Pegoraro, F., Bulanov, S.V. (2000). Impact of kinetic processes on the macroscopic nonlinear evolution of the electromagnetic-beam-plasma instability. *Phys. Rev. Lett.* 84, 3602-3605

Cheng, C.Z., Knorr, G. (1976). The integration of the Vlasov equation in configuration space. *J. Comp. Phys.* 22, 330-351

Crouseilles, N., Respaud, T., Sonnendrücker, E. (2009). A forward semi-Lagrangian method for the numerical solution of the Vlasov equation. *Comp. Phys. Comm.* 2009, 180, 1730-1745

Dawson, J.M., Shanny, R. (1968). Some investigations of Nonlinear behaviour in one-dimensional plasmas.*Phys. Fluids* 11, 1506-1523

Denavit, J., Kruer, W.L. (1971). Comparison of Numerical Solutions of the Vlasov equation with particle simulations of collisionles Plasmas. *Phys. Fluids* 14, 1782-1791

Doveil, F., Firpo, M.-C., Elskens, Y., Guyomarc'h, D., Poleni, M., Bertrand, P (2001). Trapping oscillations, discrete particle effects and kinetic theory of collisionless plasma. *Phys. Lett. A* 284, 279-285

Eliasson, B., Shukla, P.K. (2006). Formation and dynamics of coherent structures involving phase-space vortices in plasmas. *Phys. Rep.* 422, 225-290

Gagné, R., Shoucri, M. (1977). A splitting scheme for the numerical solution of the Vlasov equation. *J. Comp. Phys.* 24,445-449

Ghizzo, A., Shoucri, M.M., Bertrand, P., Feix, M., Fijalkow, E. (1988). Nonlinear evolution of the beam-plasma instabilities. *Phys. Lett.* A, 129, 453-458

Joyce, G., Knorr, G., Burns, T. (1971). Nonlinear behavior of the one-dimensional weak beam plasma system. *Phys. Fluids* 14, 797-801

Knorr, G. (1977). Two-dimensional turbulence of electrostatic Vlasov plasmas. *Plasma Phys.* 19, 529-538

Manfredi, M., Shoucri, M., Shkarofsky, I., Ghizzo, A., Bertrand, P., Fijalkow, E., Feix, M., Karttunen, S., Pattikangas, T., Salomaa, R. (1996). Collisionless diffusion of particles and current across a magnetic field in beam/plasma interaction. *Fusion Tech.* 29, 244-260

Nakamura, T.,Yabe, T. (1999). Cubic interpolated propagation scheme for solving the hyper-dimensional Vlasov-Poisson equation in phase-space. *Comput. Phys. Comm.* 120, 122-154

Nührenberg, J. (1971). A difference scheme for Vlasov's equation. *J. Appl. Math. Phys.* 22, 1057-1076

Okuda, H., Horton, R., Ono, M., Wong, K.L. (1985). Effects of beam plasma instability on current drive via injection of an electron beam into a torus. *Phys. Fluids* 28, 3365-3379

Pohn, E., Shoucri, M., Kamelander, G. (2005). Eulerian Vlasov codes. *Comm. Comp. Phys.* 166, 81-93

Schamel, H. (2000). Hole equilibria in Vlasov-Poisson systems: A challenge to wave theories of ideal plasmas.*Phys.Plasmas* 7, 4831- 4844

Shoucri, M. (1979). Nonlinear evolution of the bump-on-tail instability. *Phys. Fluids* 22, 2038-2039

Shoucri, M.(2008). *Numerical Solution of Hyperbolic Differential Equations*, Nova Science Publishers Inc.,New-York.

Shoucri, M.(2009). The application of the method of characteristics for the numerical solution of hyperbolic differential equations,In: *Numerical Solution of Hyperbolic Differential Equations*, S.P. Colombo,(Ed.), Nova Science Publishers, New-York.

Shoucri, M. (2010). The bump-on-tail instability, In: *Eulerian codes for the numerical solution of the kinetic equations of plasmas,* M. Shoucri, (Ed.), p. 291, Nova Science Publishers, New York.

Sircombe, N.J., Dieckman, M.E., Shukla, P.K., Arber, T.D. (2006). Stabilisation of BGK modes by relativistic effects. *Astron. Astrophys.452,* 371-382

Sircombe, N.J., Bingham, R., Sherlock, M., Mendonca, T., Norreys, P. (2008). Plasma heating by intense electron beams in fast ignition. *Plasma Phys. Control. Fusion* 50, 065005-(1-10)

Umeda, T., Omura, Y., Yoon, P.H., Gaelzer, R., Matsumoto, H. (2003). Harmonic Langmuir waves.III.Vlasov simulation. *Phys. Plasmas* 10, 382-391

Valentini, F., Carbone, V., Veltri, P., Mangeney, A. (2005). Wave-particle interaction and nonlinear Landau damping in collisionless electron plasmas. *Trans. Theory Stat. Phys.* 34, 89-101



Numerical Simulations - Applications, Examples and Theory
Edited by Prof. Lutz Angermann

ISBN 978-953-307-440-5
Hard cover, 520 pages
Publisher InTech
Published online 30, January, 2011
Published in print edition January, 2011

This book will interest researchers, scientists, engineers and graduate students in many disciplines, who make use of mathematical modeling and computer simulation. Although it represents only a small sample of the research activity on numerical simulations, the book will certainly serve as a valuable tool for researchers interested in getting involved in this multidisciplinary ï¬eld. It will be useful to encourage further experimental and theoretical researches in the above mentioned areas of numerical simulation.

How to reference
In order to correctly reference this scholarly work, feel free to copy and paste the following:

Magdi Shoucri (2011). Numerical Simulation of the Bump-on-Tail Instability, Numerical Simulations - Applications, Examples and Theory, Prof. Lutz Angermann (Ed.), ISBN: 978-953-307-440-5, InTech, Available from: http://www.intechopen.com/books/numerical-simulations-applications-examples-and-theory/numerical-simulation-of-the-bump-on-tail-instability

INTECH
open science | open minds

InTech Europe
University Campus STeP Ri
Slavka Krautzeka 83/A
51000 Rijeka, Croatia
Phone: +385 (51) 770 447
Fax: +385 (51) 686 166
www.intechopen.com

InTech China
Unit 405, Office Block, Hotel Equatorial Shanghai
No.65, Yan An Road (West), Shanghai, 200040, China
中国上海市延安西路65号上海国际贵都大饭店办公楼405单元
Phone: +86-21-62489820
Fax: +86-21-62489821

© 2011 The Author(s). Licensee IntechOpen. This chapter is distributed under the terms of the Creative Commons Attribution-NonCommercial-ShareAlike-3.0 License, which permits use, distribution and reproduction for non-commercial purposes, provided the original is properly cited and derivative works building on this content are distributed under the same license.

IntechOpen

IntechOpen